Yellow Fever Virus Interactomes Reveal Common and Divergent Strategies of Replication and Evolution for Mosquito-borne Flaviviruses

Matthew W. Kenaston[1,†], Liubov Cherkashchenko[1,#], Chase L. S. Skawinski[2,#], Adam T. Fishburn[1], Vardhan Peddamallu[2], Cole J. Florio[1], Avery E. Robertson[1], Tamanash Bhattacharya[3], Janet M. Young[3], Harmit S. Malik[3,4], Priya S. Shah[1,2*]

[1] Department of Microbiology and Molecular Genetics, University of California, Davis, CA

[2] Department of Chemical Engineering, University of California, Davis, CA

[3] Division of Basic Sciences, Fred Hutchinson Cancer Center, Seattle, WA

[4] Howard Hughes Medical Institute, Fred Hutchinson Cancer Center, Seattle, WA

[†] Present address: Mayo Clinic Alix School of Medicine, Phoenix, AZ

[#] These authors contributed equally

* Corresponding and lead author, prsshah@ucdavis.edu

Abstract

Pathogenic mosquito-borne flaviviruses infect mosquito and human hosts, relying on host protein interactions to replicate, evade immunity, and mediate pathogenesis. Prior proteomic studies mapped such interactions for some flaviviruses, but yellow fever virus (YFV)—a pathogen of resurgent concern—remains understudied. Here, we map YFV interactomes in human and mosquito cells to identify interactions common among divergent flaviviruses or unique to YFV. Functional assays reveal a previously unrecognized YFV restriction factor: RBBP6 inhibits YFV genome replication by interacting with the viral polymerase NS5. We enhance the identification of dual-host interactions using structural modeling and holistic network integration. Extending our holistic approach to other flavivirus interactomes, we distinguish conserved mechanisms of host targeting from those unique to YFV. Contrary to expectations that conserved viral proteins lead to conserved protein interactions, we find that Capsid, a divergent structural protein, shares more host interactions than NS5, a conserved enzyme. Integrating proteomics with complementary analyses defines new principles of host-targeting strategies across flavivirus and host evolution, offering a versatile resource for navigating the complex landscape of flavivirus biology.

Keywords: yellow fever virus, flaviviruses, virus-host interaction, integrative proteomics, systems biology, virus-host evolution

33 # Introduction

34 Mosquito-borne orthoflaviviruses (commonly known as flaviviruses) pose a serious and
35 increasing threat to public health worldwide with their continued re-emergence in the past decade.
36 These positive-sense RNA viruses, which includes dengue virus (DENV), Zika virus (ZIKV), West
37 Nile virus (WNV), and yellow fever virus (YFV), contributes to hundreds of millions of human
38 infections worldwide every year[1]. Due to ongoing climate change, the geographical range of
39 common vectors, such as the *Aedes aegypti* mosquito, is rapidly expanding[2,3]. Human
40 urbanization and encroachment have further exacerbated this trend[4,5]. And yet, there are only
41 limited vaccine strategies and no approved antivirals for flaviviruses[6]. Thus, it is critical to unravel
42 the molecular mechanisms governing flavivirus replication.

43 Identifying virus-host protein-protein interactions (PPIs) is crucial for developing both
44 virus- and host-targeted therapies[7]. Flaviviruses have small RNA genomes that encode a single
45 polyprotein, which is subsequently proteolytically processed into 10 viral proteins. Three of these
46 proteins—Capsid, prM (membrane precursor), and Envelope—are structural components of the
47 virion, while the remaining non-structural (NS) proteins facilitate replication, translation, assembly,
48 and viral egress. These viral proteins use physical interactions with host proteins to hijack cellular
49 machinery essential for viral replication, immune evasion, and pathogenesis[8]. Previous studies
50 have applied proteomics-based approaches to identify virus-host PPIs across vertebrate and
51 invertebrate host cells[9,10], offering new strategies for vector control and therapeutic targets.

52 Due to their severe disease burdens or alarming pathogenesis, flaviviruses like DENV and
53 ZIKV have been the focus of many previous studies[11]. In contrast, YFV has yet to be studied using
54 contemporary proteomic techniques. This is partly because a robust live attenuated vaccine[12] can
55 provide long-term immunity[13], reducing the perceived threat of YFV. However, limited vaccine
56 availability and efficacy combined with unexpected increases in mosquito vector competency
57 have led to repeated YFV outbreaks in the last decade[14–16]. YFV was estimated to cause 109,000

58 severe infections and 51,000 deaths in 2018 alone[17]. More recently, a Pan-American Health
59 Organization alert in February 2025 reported an alarming increase in YFV cases in the Americas,
60 prompting urgent recommendations for enhanced protection[18]. Recent surveillance also suggests
61 YFV range is expanding[19]. Considering this resurgence, understanding the molecular
62 mechanisms of YFV replication and pathogenesis has regained urgency and relevance.

63 YFV is an important virus to consider from an evolutionary perspective. YFV is
64 phylogenetically distinct from DENV, ZIKV, and WNV[20,21], flaviviruses whose host interactions
65 have been studied in depth[22–24]. DENV, ZIKV, and WNV are more closely related to each other
66 than to YFV. However, DENV, ZIKV, and YFV can all use *A. aegypti* as a vector and use primates
67 as vertebrate reservoirs, whereas WNV employs *Culex* mosquitoes as vectors and birds as
68 amplifying vertebrate reservoirs[1]. Analyzing YFV-host PPIs thus represents a powerful
69 opportunity to understand the biology of an understudied and biomedically relevant flavivirus while
70 also revealing unique and broadly conserved features of flavivirus biology across different
71 flavivirus-host PPI datasets.

72 Here, we conduct comprehensive proteomics analyses to construct YFV-host PPI
73 networks in both human and mosquito (*A. aegypti*) cells. Using a targeted CRISPRi knockdown
74 screen of YFV-interacting human proteins, we identify the E3 ubiquitin ligase RBBP6
75 (retinoblastoma binding protein 6) as a novel YFV restriction factor. We integrate computational
76 approaches, including evolutionary conservation metrics, AI-based structural modeling, and high-
77 dimensional network-based analyses, to systematically evaluate the breadth of flavivirus-host
78 PPIs across hosts and viruses. Our studies improve the identification of shared interactions
79 across divergent hosts and reveal general flaviviral strategies as well as YFV-specific interactions
80 that reflect YFV's divergence from other flaviviruses. Finally, by integrating PPI studies across
81 four flaviviruses, we discover a counterintuitive trend regarding the conservation of virus-host
82 PPIs. The conservation of flavivirus proteins is inversely correlated with the conservation of their
83 host interactomes, raising interesting questions regarding the speed at which some highly

84 conserved flavivirus proteins can evolve new protein interactions. By integrating multiple
85 proteomic datasets with orthogonal experimental and computational approaches, we create a
86 multidimensional resource for understanding host interactions, replication strategies, and
87 evolution of mosquito-borne flaviviruses.

88 Results

89 *A YFV-Human Interactome*

90 To map the YFV-human PPI network, we employed a proteomics-based approach using
91 affinity purification-mass spectrometry (AP-MS). We first cloned protein-coding sequences from
92 the Asibi strain of YFV (YFV-Asibi) with C-terminal 2xStrep affinity tags. Following transient
93 expression in HEK293T cells, we performed affinity purification and confirmed the expression and
94 purification of both viral baits and co-purified host proteins (Figures 1A and S1A). We used LC-
95 MS/MS to analyze eluted proteins. Replicate samples associated with specific viral baits showed
96 strong correlations with each other but not with samples from other viral baits, indicating
97 reproducibility and specificity (Figure S1B). To score these interactions, we applied a tiered
98 computational approach, integrating Mass Spectrometry Interaction STatistics (MiST) and
99 Significance Analysis of INTeractome (SAINT) (Table S1). We identified 309 high-confidence
100 PPIs (HC-PPIs) spanning 10 YFV baits (Figure 1B). We only failed to identify HC-PPIs for prM
101 protein, which also had few interactions in past studies of other flaviviruses using a similar
102 approach[22,23].

103 To broadly assess the functional relevance of YFV-human PPIs, we performed enrichment
104 analyses on the HC-PPIs associated with each viral protein using Gene Ontology: Biological
105 Process (GO:BP) and Reactome pathway analyses (Figure 1C and Table S1). These analyses
106 revealed the broad targeting of host processes previously shown to be critical for flavivirus
107 replication and pathogenesis[9], including RNA metabolism[25–27], chromatin modification and

108 remodeling[22,28], ER stress response[29], and cell trafficking and organization[30,31]. NS5 and Capsid
109 exhibited strong enrichment for nuclear processes, such as RNA splicing, antiviral defense, and
110 ribosome biogenesis, consistent with their previously characterized nuclear functions[28,32–35].
111 NS4A and NS2A primarily targeted pathways related to membrane dynamics, including protein
112 insertion into membranes and ER organization[36,37]. NS3 and NS2B3 showed distinct yet
113 complementary enrichment patterns, with NS2B3 favoring endosomal pathways and NS3
114 interacting with ubiquitination and protein folding machinery. We found that prME, the protein
115 complex of the Envelope (E) with its chaperone prM, is uniquely associated with pathways
116 involved in virion assembly, potentially reflecting its role in flavivirus particle maturation. The
117 subcellular localization of host proteins involved in HC-PPIs also correlated well with our observed
118 subcellular localizations of the respective flavivirus proteins (Figures 1D and S2). To contextualize
119 our investigation and provide visualization, we constructed a network of YFV-human HC-PPIs
120 annotated with GO:BP and CORUM protein complexes[38] (Figure 2). This network provides a
121 comprehensive resource for understanding YFV-human interactions.

122 *RBBP6 is a Novel Inhibitor of YFV Genome Replication*

123 Genome-wide screening approaches for host dependency factors have revealed many
124 important details of flavivirus replication[35,37,39–42]. We compared our YFV-human HC-PPIs with a
125 recent YFV-focused genome-wide CRISPR screen that identified host dependency factors in
126 human cells[35]. We identified a significant overlap ($p = 2.8x\ 10^{-14}$) of 19 host factors among our
127 277 unique prey and the top 1% of YFV host dependency factors (Figure 2). This suggests our
128 HC-PPIs are enriched for host proteins involved in YFV replication. However, this is likely an
129 underestimate, since many flavivirus host factors cannot be studied using pooled genome-wide
130 approaches due to their inherent limitations, such as the selection criteria and the targeting of
131 essential genes. Proteomics-based interactomes offer a powerful complementary approach to

132 genome-wide screens, providing a targeted set of host genes to assess the impacts on viral
133 replication.

134 To further dissect the functional consequences of promising YFV-host interactions, we
135 performed a targeted CRISPR interference (CRISPRi) screen of 18 host proteins from our YFV-
136 human HC-PPI network. We modified our experimental setup in two ways compared to our
137 proteomics assays. First, we used the 17D strain of YFV (YFV-17D), a biosafety level 2 strain that
138 is more amenable to infection-based screening. Despite serial passaging, only 32 amino acids
139 differentiate the entire polyproteins of YFV-17D and YFV-Asibi[43]. Thus, YFV-17D retains a high
140 degree of sequence similarity to YFV-Asibi, which was used to generate our proteomic data.
141 Second, since the liver is a major site of YFV replication[44–46], we carried out our screen in
142 hepatocyte-derived Huh7 cells instead of the HEK293T cells used for proteomics.

143 Using transient CRISPRi knockdown in Huh7-dCas9 cells, we assessed the effect of host
144 protein depletion on YFV-17D titers. We individually targeted each host gene with two unique
145 guide RNAs (gRNAs); most gRNAs achieved efficient knockdown (>70%). We proceeded with
146 any gRNAs that reached at least 50% knockdown relative to the non-targeting negative control
147 (ncgRNA) (Figure 3A). Knockdown cells were then infected with YFV-17D at a multiplicity of
148 infection (MOI) of 0.1, and infectious viral titers were quantified by plaque assay at 48 hours post-
149 infection (hpi). We observed strong reproducibility across three biological replicates, with a
150 Pearson's correlation coefficient (R) ranging from 0.62 to 0.80. Overall, 10 of 30 tested gRNAs
151 (33%), targeting 7 unique genes, significantly influenced YFV titers (Figure 3B and Table S2,
152 |robust Z-score| > 2). Our findings are consistent with previous studies examining host factors
153 involved in flavivirus replication[23]. Viral replication decreased in two knockdowns targeting two
154 unique host genes (robust Z-score < -2), suggesting these host genes encode dependency
155 proteins that perform proviral functions. In contrast, 8 knockdowns targeting 5 unique host genes
156 resulted in increased viral replication (robust Z-score > 2); these host genes likely represent
157 antiviral factors that restrict viral replication.

158 Most striking among the putative restriction factors was RBBP6. A >75% reduction in
159 RBBP6 expression (Figure 3A) resulted in up to 60-fold increase in YFV titers for two different
160 gRNAs across multiple MOIs (Figure 3C). This suggests that RBBP6 potently restricts YFV
161 replication. RBBP6 is an E3 ubiquitin ligase that regulates RNA 3' end processing, the cell cycle,
162 and embryonic development[47–49]. Our PPI analyses revealed that RBBP6 interacts with YFV NS5
163 (Figure 2), which encodes the RNA-dependent RNA polymerase (RdRP) and methyltransferase
164 (MTase). Both YFV NS5 and RBBP6 can localize to the nucleus (Figure 3D). To validate this
165 interaction during infection, we performed endogenous RBBP6 immunoprecipitation (IP) in YFV-
166 17D-infected Huh7 cells. Western blotting revealed that NS5 co-precipitated with RBBP6 (Figure
167 3E). Additionally, treating IP samples with RNaseA substantially decreased the amount of NS5
168 that could be co-immunoprecipitated with RBBP6, indicating the interaction is stabilized by RNA
169 (Figure 3E).

170 Next, we used domain deletions to map the domains of RBBP6 responsible for this
171 interaction (Figure 3F). Although full-length RBBP6 was poorly expressed, smaller RBBP6
172 domains were expressed well (Figure 3G). Co-IP analyses revealed that both the Proline-Rich
173 (Pro-RS) and p53-binding domains were independently sufficient for interaction with NS5 (Figure
174 3G). Confocal immunofluorescence microscopy revealed clear nuclear localization for the Pro-
175 RS domain; however, the p53-binding domain had a cytoplasmic localization (Figure S3A-C). We
176 propose that YFV NS5 interaction with the p53 domain of RBBP6 may be facilitated by NS5
177 nucleocytoplasmic shuttling (Figures S2A and S3D-F).

178 We also mapped the NS5 domains required for interaction with RBBP6 by co-IP assays.
179 While full-length NS5 interacts with RBBP6, neither the MTase (residues 1 to 261) nor RdRP
180 (residues 262 to 909) domain was sufficient to pull down RBBP6 (Figure 3H, Figure S3D). No
181 YFV NS5 truncations were excluded from the nucleus, suggesting that their lack of interaction
182 with RBBP6 was unrelated to subcellular mislocalization (Figure S3D-F). Our findings suggest
183 that YFV NS5 requires an intact conformation or the presence of multiple domains to bind RBBP6.

184 NS5 encodes for the viral RdRP and MTase, and is therefore essential for viral RNA
185 synthesis. We tested whether RBBP6 depletion enhanced YFV genome replication using a
186 replicon encoding a luciferase reporter[50]. The flavivirus life cycle is characterized by an initial
187 phase of translation, in which little to no increase in reporter activity is observed, followed by a
188 switch to replication, during which reporter activity increases dramatically. Depletion of RBBP6
189 resulted in minor but significant increases in reporter activity during the early translation phase
190 and a more pronounced and sustained ~10- to 70-fold increase in reporter activity during the
191 replication phase (Figure 3I). Together, our data support a model in which RBBP6 acts as a YFV
192 restriction factor by inhibiting YFV genome replication through a complex RNA-mediated
193 interaction with NS5.

194 Positive selection is often observed in other antiviral restriction factors at their interface
195 with viral targets due to an arms race for binding affinity or evasion from binding[51–54]. However,
196 analysis of 28 primate *RBBP6* sequences revealed no significant evidence of positive selection
197 (Table S3). This lack of positive selection might reflect a lack of significant coevolution between
198 flaviviruses and primate *RBBP6* or constraints on *RBBP6* to maintain its essential host functions.

199 *A Structure-based and Holistic Approach to Identify Interacting Homologs*

200 Mosquito-borne flaviviruses must replicate in both vertebrate and invertebrate hosts for
201 their transmission. They do so by hijacking host processes across evolutionarily distinct cellular
202 environments[37,40]. To identify how YFV proteins commandeer mosquito cells, we constructed a
203 YFV-mosquito interactome following the same steps as our YFV-human network, except that we
204 expressed YFV proteins in *A. aegypti* Aag2-AF5 cells[55] (Figure S1C). We identified YFV-mosquito
205 HC-PPIs using the same AP-MS and computational scoring pipeline previously employed for
206 human cells, ensuring comparability across datasets (Figures 1A and S1D, and Table S4).
207 Despite lower detection sensitivity in mosquito cells, we identified robust interactions for most
208 YFV proteins (Figure 4A). The only exceptions were prM and prME, which failed to express in

209 Aag2-AF5 cells (Figure S1C). Furthermore, although NS1 and NS2B were expressed well, none
210 of their interactions met our scoring threshold. In total, we identified 150 YFV-mosquito HC-PPIs
211 across 7 viral baits (Figure 4A).

212 In addition to host-specific targeting, our previous study with DENV showed that
213 flaviviruses can also target homologous proteins and processes across human and mosquito
214 cells[22]. Our YFV-host proteomics in human and mosquito cells can similarly reveal such
215 interacting homologs (interologs) or interologous processes, utilizing evolutionary relationships
216 between hosts. Comparing YFV-human and YFV-mosquito interactomes revealed 14 interologs
217 at the protein level and an additional 12 complex and pathway-level interologs (Figure S4A).

218 Given our limited ability to identify direct interologs using evolutionary relationships, we
219 hypothesized that conserved host protein structures might provide a complementary way to
220 measure flavivirus PPI conservation across hosts. To test this, we leveraged recent AI-driven
221 structure prediction and alignment tools to expand interolog identification (Figure S4B). Our
222 workflow used Foldseek[57,58] and FATCAT[59] to perform protein structure alignments on the
223 AlphaFold2-predicted structures of the human and *A. aegypti* proteomes. Foldseek and FATCAT
224 output familiar structure similarity scores (*e.g.,* TM-score or RMSD) using complementary
225 approaches. Foldseek uses a 3D alphabet to simplify structural complexity. This enables fast,
226 scalable alignments with large numbers of structures. In contrast, FATCAT flexes proteins into an
227 optimal overlaid structure (superimposition) that maximizes alignment length one residue pair at
228 a time. Combining these analyses enables the simplification of large-scale comparisons into
229 direct, representative alignments without compromising on sensitivity or computational cost.

230 We first performed proteome-wide rigid structural alignments using Foldseek. To account
231 for potential biases in AlphaFold2 predictions, we supplemented these structural homologs with
232 evolutionary homologs from inParanoid8[60]. Each selected pair then underwent flexible alignment
233 with FATCAT. After overlaying these with the HC-PPIs from YFV and DENV, our structure-based

234 approach increased the number of YFV interologs from 14 to 21 and the number of DENV
235 interologs from 10 to 14 (Figure 4C, Table S5).

236 However, we were surprised to find no overlap between YFV and DENV interologs. This
237 lack of overlap could be due to fundamentally different dual-host strategies between YFV and
238 DENV. Alternatively, the lack of overlap could stem from technical differences in protein
239 identification and scoring. Indeed, many functionally relevant host interactions may fall below
240 conventional scoring thresholds as “near misses” in one HC-PPI network or another, leading to
241 an underestimation of conserved interactions, processes, and pathways[9,61–64]. To overcome these
242 limitations, we adopted a computational pipeline developed by Gordon and colleagues to evaluate
243 virus-host interactomes holistically beyond strict scoring cutoffs[64]. Across the YFV-human, YFV-
244 mosquito, DENV-human, and DENV-mosquito datasets, we performed hierarchical clustering on
245 MiST scores. We focused our analysis on viral baits studied across all four datasets (Capsid,
246 NS3, NS2B3, NS4A, NS5) and only included data if the bait-prey pair was a HC-PPI in at least
247 one of the four datasets analyzed. With this approach, we found 8 interaction clusters, one of
248 which represents interactions shared across both viruses and both hosts (Figure 4C). This
249 suggests that YFV and DENV indeed share at least some conserved dual-host strategies.
250 Extracting this pan-flavivirus and interologous cluster for enrichment analysis (Figure 4D), we
251 found that individual flavivirus proteins targeted distinct host processes. The Capsid protein
252 targeted translation, ribosome biology, and RNA splicing. NS5 targeted the response to virus and
253 protein localization to the cytoplasmic stress granule, both of which are implicated in flavivirus
254 replication[32,65–69]. NS2B3 interactions were enriched for protein phosphorylation and
255 mitophagy[70,71]. Finally, NS4A expectedly targeted organelle organization, transport, and
256 glycosylation-related pathways. Thus, holistic analysis improves the identification of hijacked
257 pathways fundamental to the dual-host nature of mosquito-borne flaviviruses.

258 Viruses often exploit these highly conserved host functions to ensure replication, thereby
259 avoiding evolutionary barriers, as hosts also rely on these critical pathways for cellular function.

260 We speculated that targeting these highly conserved systems is especially important for dual-host
261 viruses, such as mosquito-borne flaviviruses, and thus they are targeted as interologs. We
262 compared HC-PPIs and interologs against the entire set of human-mosquito homologous pairs to
263 assess sequence conservation. HC-PPIs showed significantly higher sequence identity compared
264 to homologs in general (Figure 4E, Table S5). This suggests that YFV and DENV evolved to target
265 conserved host proteins, as expected[72]. Our complete set of interologs also showed significantly
266 higher sequence identity compared to homologs in general, yet interologs did not have higher
267 sequence identity than HC-PPIs (Figure 4E, Table S5).

268 While viruses often target conserved host proteins, as we observed with our HC-PPIs and
269 interologs, these protein interaction surfaces can also contain rapidly evolving sites that serve to
270 break and re-establish virus-host interactions[51–54,56]. So, we explored whether any of the YFV
271 interologs exhibit evidence of participation in this evolutionary arms race. Since there are too few
272 *Aedes* genome assemblies available for analysis, we used simian primate genomes to search for
273 signatures of positive selection (Table S3). *MRPS9* showed strong evidence for positive selection.
274 *DDX21*, *NOP53,* and *MRPS31* showed weaker and less consistent signatures of rapid evolution.
275 Our findings suggest that, although they are enriched for conservation, interologs are not uniquely
276 defined by it, and some may still participate in evolutionary arms races. This highlights the balance
277 between functional constraint and adaptive flexibility that shapes flavivirus-host interactions
278 across host species.

279 *High-Dimensional Analysis Refines Pan-flavivirus and Divergent Interactions*

280 Previous phylogenetic analysis has shown that YFV is evolutionarily distant from other
281 mosquito-borne flaviviruses, such as DENV, WNV, and ZIKV[20,21] (Figure 5A). Thus, our YFV
282 dataset provides a powerful foundation for identifying both virus-host interactions specific to YFV
283 and those that are broadly conserved among mosquito-borne flaviviruses. To contextualize these
284 interactions, we compared our YFV-human network to previous studies that used a comparable

285 methodology to identify flavivirus-human PPIs for DENV (serotype 2, strain 16681), ZIKV (strains
286 H/PF/2013 [ZIKVfp] and MR766 [ZIKVug]), and WNV (strain NY 2000-crow 3356)[22,23]. The direct
287 overlap between these datasets only represented ~5-10% of YFV HC-PPIs (Figure S5A).
288 However, since a holistic analysis that captured "near-misses" was useful for our integration of
289 datasets across multiple hosts (Figure 4C-D), we applied the same technique here. Across the
290 five flavivirus-human PPI datasets, we performed hierarchical clustering on MiST scores for viral
291 baits studied across all four datasets (Capsid, NS3, NS2B3, NS4A, NS5). Again, we performed
292 analysis on bait-prey pairs that were a HC-PPI in at least one of the five datasets analyzed. Our
293 holistic analysis identified 17 interaction clusters (Figure 5B), including conserved interactions
294 across all flaviviruses (cluster 3), YFV-specific interactions (cluster 1), or interactions conserved
295 across all viruses except YFV (YFV-excluded, cluster 8).

296 To better understand the cellular processes involved in pan-flavivirus PPIs, we performed
297 enrichment analyses on cluster 3 (Figure 5C). Capsid interactions with host proteins dominated
298 this cluster, revealing conserved enrichment of translational processes, mRNA modification, and
299 ribosome biogenesis. Host protein interactions with non-structural proteins were also represented
300 in the conserved interactions. NS3 interactors enriched for protein folding, ubiquitination, and
301 stress response. NS4A interactors enriched for proteins involved in membrane organization and
302 protein transport, reflecting its known role in rearranging ER membranes to form replication
303 complexes[73,74]. NS5 interactors enriched for processes related to RNA splicing, reflecting its
304 known role in perturbing host gene expression[33]. Only NS2B3 interactions did not show
305 enrichment for any biological processes. As with Gordon et al[64], our analyses confirm that a high-
306 dimensional approach surpasses the limitations of scoring thresholds or single-virus datasets,
307 revealing host targets conserved across these mosquito-borne flaviviruses and related to
308 fundamental aspects of flavivirus biology.

309 The YFV-specific interactions (cluster 1) and YFV-excluded interactions (cluster 8)
310 suggest an evolution of distinct host hijacking strategies across the flavivirus phylogeny. We

311 therefore evaluated whether these opposing sets of PPIs could be used to understand the
312 evolutionary divergence of YFV relative to other mosquito-borne flaviviruses. To that end, we
313 calculated differences between YFV MiST scores and those of every other flavivirus in the dataset
314 (DENV, ZIKV [we chose to focus on ZIKVfp for simplicity], and WNV). This generated a distribution
315 of differential interaction scores (DIS) relative to YFV for each viral bait. In this YFV-centric
316 approach, a positive DIS indicates the PPI scored highly for YFV relative to the other flavivirus, a
317 negative DIS indicates the PPI scored poorly for YFV, while a near-zero DIS indicates the PPI
318 scored equally in both datasets (Figure 5D).

319 When visualizing DIS distributions, several trends related to specific viral proteins became
320 apparent (Figure 5E). Capsid interactions were predominantly associated with neutral or negative
321 DIS, suggesting YFV Capsid has many interactions that are shared with other flaviviruses, few
322 YFV-specific interactions, and lacks many of the host interactions observed for other flaviviruses.
323 In contrast, NS2B3 and NS3 exhibited predominantly positive DIS, indicating these proteins have
324 mostly YFV-specific interactions with few shared interactions with other flaviviruses. NS4A and
325 NS5 showed greater variability in their DIS distributions with shared, YFV-specific, and YFV-
326 excluded interactions. We computed Pearson's correlation coefficients between each pairwise
327 distribution of DIS values and observed consistently high correlations (>0.7, Figure S5B). This
328 suggests YFV's differential interactions represent *bona fide* divergence in host targeting patterns
329 rather than stochastic deviations in MS detection of proteins in one dataset or another.

330 To better understand the processes involved in PPIs reflecting YFV's evolutionary
331 divergence, we extracted statistically significant gene enrichments ($p < 0.05$) either for the YFV-
332 specific cluster (cluster 1) or the YFV-excluded cluster (cluster 8) (Figure 5E). We excluded any
333 processes that were significantly enriched for other clusters to ensure these processes were truly
334 unique to YFV-specific or YFV-excluded PPIs. These analyses revealed that multiple YFV
335 proteins target host processes in evolutionarily distinct ways. For example, RNA processing and
336 histone modification were significantly enriched for YFV-excluded Capsid and NS5 interactions.

337 This suggests that although other flaviviruses target these epigenetic processes through Capsid
338 and NS5, YFV does not. Conversely, YFV NS2B3 uniquely targeted host proteins in organelle
339 assembly and microtubule organizing center (MTOC) organization, YFV NS3 uniquely targeted
340 mRNA stability, and YFV NS4A uniquely targeted metal ion transport and protein
341 dephosphorylation.

342 We extended this analysis to calculate DIS relative to other flaviviruses. This revealed
343 more variable correlations and weaker enrichments for DENV-, ZIKV-, and WNV-specific
344 interactions (Figure S5C-F). This weaker signal is consistent with them being more closely related
345 to each other than YFV and thus having fewer virus-specific or virus-excluded interactions to drive
346 strong DIS scores or enrichment. Together, these results underscore that the pan-flavivirus, YFV-
347 specific, and YFV-excluded clusters represent molecular strategies of host targeting that coincide
348 with the evolution of flaviviruses. To visualize pan-flavivirus and YFV-specific HC-PPIs, we
349 incorporated annotations into our YFV-human HC-PPI visualization using annotations from
350 clusters 3 and 1, respectively (Figure S6).

351 *Flavivirus Protein Sequence Conservation Does Not Equate to Conservation of*
352 *PPIs*

353 Protein sequence conservation is often viewed as a predictor of functional
354 conservation[64,75,76]. Structural proteins, such as Capsid, typically exhibit lower sequence
355 conservation than enzymes, like NS5, leading to predictions that structural proteins will retain
356 fewer interactions across viruses. Yet, our preceding analysis using holistic integration and DIS
357 showed a surprisingly high level of conservation for Capsid interactions compared to non-
358 structural proteins (Figures 5C, 5E, and S6). We therefore tested whether the conservation of
359 viral protein sequence can reliably predict flavivirus-host PPI conservation using the four flavivirus
360 datasets (Figure 6A).

361 We calculated pairwise sequence identities and pairwise correlations of MiST scores for
362 each viral bait. Within a single viral bait, we observed a strong positive correlation between these
363 two quantities (Figure 6B). The only exception was NS3. This suggests that the conservation of
364 viral protein sequences predicts conserved virus-host PPIs for individual viral proteins. However,
365 when comparing across viral baits, we observed a slight but unexpected negative correlation
366 between MiST correlation and sequence identity (R = -0.19). This negative correlation across viral
367 baits was more pronounced when our analysis focused on HC-PPIs (R = -0.89, Figure 6C). Thus,
368 surprisingly, we find that more rapidly evolving proteins exhibit higher PPI conservation relative
369 to viral proteins that evolve more slowly.

370 We investigated whether specific elements of protein structure and function could explain
371 the inverse correlation between viral protein conservation and their host PPI conservation. We
372 focused on NS5 and Capsid because they represent the extremes of PPI and sequence
373 conservation (Figure 6B-C). We first mapped conservation and enzyme activity onto their
374 structures (Figure 6D-E). NS5 is a large protein with a highly conserved core and enzyme active
375 sites. Conserved amino acids are significantly more likely to be buried in regions of low solvent-
376 accessible surface area (SASA), while variable amino acids have significantly higher SASA and
377 opportunity to engage in PPIs (Figure 6F). In contrast, Capsid is a smaller structural protein with
378 lower overall conservation, and its amino acid variation is evenly distributed across low and high
379 SASA regions (Figure 6F). We hypothesized that the enzymatic core of NS5, with high
380 conservation, low SASA, and limited opportunity to interact with host proteins, could be skewing
381 our comparison of NS5 to Capsid. To provide a fairer comparison, we considered only the 233
382 residues with the highest SASA from NS5 that provide a median of ~108.7 $Å^2$, almost identical to
383 Capsid's median SASA of 108.8 $Å^2$ (Figure 6G). This group of NS5 residues, representing the
384 most solvent-accessible regions of the protein, closely resembles Capsid in both the distribution
385 of residue identities and mean residue identities: 61% and 58% for NS5 and Capsid, respectively.
386 Despite these similar mean identities near the proteins' surfaces, NS5 still maintains a lower PPI

387 conservation compared to Capsid. Thus, NS5-host PPIs are highly sensitive to small changes in
388 amino acid identity. Our analysis highlights the power of integrating multiple related virus-host PPI
389 networks using a sequence and structure-informed approach, especially when amending a long-
390 standing hypothesis regarding the drivers of conserved virus-host PPIs.

391 # Discussion

392 In this study, we systematically mapped YFV-host interactomes in both human and
393 mosquito cells using AP-MS, thereby expanding on previous work on flavivirus-host interactions.
394 We use our YFV-human interactome analysis (Figures 1-2) and a functional screen (Figure 3) to
395 identify RBBP6 as a novel YFV restriction factor. Seeking to move beyond siloed virus-host
396 networks, we applied orthogonal approaches to analyze the data more holistically and from a
397 structural perspective. We integrated evolutionary sequence-structure relationships (Figure 4)
398 and holistic network integration (Figures 5-6) to identify novel YFV biology, and to relate virus and
399 host evolution to the evolution of virus-host PPIs, thereby providing a comprehensive resource on
400 mosquito-borne flavivirus-host interactions.

401 RBBP6's antiviral activity was also recently documented for Ebola virus (EBOV)[77]. Our
402 identification of RBBP6 as a YFV restriction factor suggests that this is a restriction factor with
403 panviral potential. Mechanistically, RBBP6 inhibits EBOV by interacting with viral protein 30
404 (VP30) to displace nucleoprotein (NP) and suppress viral transcription. Similarly, RBBP6 interacts
405 with YFV NS5 and reduces viral genome replication (Figure 3). The RNA-stabilized interaction
406 mechanism is reminiscent of other virus-host molecular interfaces that are also RNA-mediated,
407 such as the interaction between human APOBEC3G and the Vif protein of HIV-1, where RNA
408 might help serve as a 'molecular glue'[78,79]. The interaction mechanism between NS5 and RBBP6
409 is distinct from its interaction with EBOV VP30, which binds RBBP6 via a short PxY motif in the
410 Pro-RS domain of RBBP6[77]. However, RBBP6 may still serve as a competitive binder to NS5 to
411 displace NS3, as it does with NP binding to VP30.

412 Our YFV interactome also provides a starting point for dissecting molecular mechanisms
413 of viral pathogenesis. For example, RBBP6 pathogenic variants increase the risk of myo-
414 proliferative neoplasms, which can involve hemorrhaging, thrombocytosis, and coagulopathy[80,81],
415 similar to severe YF. This link between RBBP6 and hereditary and viral disease is reminiscent of
416 previous findings connecting hereditary and ZIKV-induced microcephaly[22,82]. Extending this
417 beyond a single interaction, an integrative framework enables broader comparisons not only
418 across related viruses but also across shared pathologies. YFV and EBOV share viscerotropic
419 and hemorrhagic pathologies[83] that may be derived from shared interactions with host proteins,
420 such as RBBP6. Indeed, when comparing HC-PPIs from YFV and EBOV datasets, we identified
421 21 shared interactions—a statistically significant overlap ($p = 8.5e-17$, Fisher's exact test, Figure
422 S7). These findings highlight how viruses with overlapping tropism and pathogenesis may be
423 driven by co-opting similar host factors, even when the viruses are highly evolutionarily divergent
424 from each other.

425 On the host side, a network-based holistic clustering of YFV and DENV datasets identified
426 interologs conserved across both viruses (Figure 4). This overlap was not revealed through
427 traditional analysis of HC-PPIs, and reinforces the advantages of a holistic analysis that is not
428 subject to strict scoring thresholds. The positive selection signature of interologs, especially
429 mitochondrial ribosomal proteins, is also intriguing given their interaction with flavivirus Capsid in
430 multiple datasets, enrichment in our interolog analysis (Figure S4D), and established roles in
431 promoting the replication of other viruses[84]. Thus, the positively selected genes *MRPS9* and
432 *MRPS31* may be involved in dual-host hijacking, resulting in an unanticipated evolutionary conflict
433 between flaviviruses and their hosts.

434 We extended our holistic network integration to identify pan-flavivirus and YFV-specific
435 interactions through high-dimensional network integration and differential scoring. We quantified
436 how viral proteins exhibit distinct evolutionary trajectories, retaining some interactions across
437 viruses while diverging in others. This approach was first developed and applied to coronaviruses

438 and different strains of influenza A virus (IAV), revealing the convergence and divergence of viral
439 pathogenic mechanisms[62,64,76]. Our application of this method highlights how binary interaction
440 mapping can benefit from multidimensional data analysis and viewing virus-host protein
441 interactions through the lens of virus evolution.

442 Finally, by integrating viral protein and PPI conservation with viral protein structure, we
443 revealed distinct insights into flavivirus-host interactions and their potential for evolution. A long-
444 standing assumption in molecular virology is that conserved viral proteins inherently maintain
445 conserved host interactions. Indeed, recent work on other virus families reinforced the expected
446 positive correlation between the conservation of protein sequence and interaction across distinct
447 viral proteins[64,72,76]. Our findings challenge this long-standing assumption, exemplified by the
448 contrast between NS5 and Capsid evolutionary and PPI conservation (Figure 6). Such a
449 divergence suggests that although NS5 is slowly evolving, it can nevertheless rapidly acquire new
450 interactions since small changes in surface-exposed amino acids of NS5 lead to large changes
451 in its protein interactions. Conversely, despite its rapid changes, Capsid is still able to retain
452 conserved PPIs. Whether flaviviruses are unique in this regard remains an open question that
453 can only be answered by continued comprehensive studies of virus-host PPIs.

454 In summary, we elucidated specific mechanisms of YFV replication as well as the impact
455 of both flavivirus and host evolution on flavivirus-host protein interactions, all stemming from two
456 core proteomics datasets. Yet, this was only possible through the integration of multiple
457 comprehensive flavivirus-host PPI studies and the application of complementary analyses to
458 combine functional assays, virus and host evolution, protein structure prediction, and holistic
459 network integration. Our work adds to an existing body of literature where proteomics provides a
460 powerful foundation to rapidly unravel how viruses engage with host systems through
461 PPIs[22,24,64,85–89]. Its future potential increasingly lies in its integration with orthogonal approaches[9].
462 Mosquito-borne flaviviruses exemplify the value of this approach because they must navigate

interactions across humans and mosquitoes. In the future, complementary methodologies will therefore be paramount to fully describe such adaptation strategies.

Limitations of this study

Although our study provides a comprehensive YFV-host interactome with several orthogonal approaches, the following limitations should be considered. First, despite integrating structural modeling to address annotation gaps, interolog prediction remains constrained by biases in available host protein structures and their prediction. This may lead to an under- or over-representation of certain interologs. Second, our functional validation was limited to a subset of high-confidence interactions focusing on YFV replication phenotypes, meaning that biologically relevant PPIs may have been overlooked. This could be extended by holistically analyzing our dataset against other viruses that share broad mechanisms of replication or pathogenesis, including other mosquito-borne flaviviruses or EBOV. Third, our proteomic analysis captures steady-state interactions through the expression of individual viral proteins but does not account for the temporal dynamics of virus-host engagement, including activation of innate immune pathways, which may shift over the course of infection. Future studies incorporating both spatial and time-resolved interactomics during infection could better resolve transient or stage-specific interactions. Additionally, since most experimental work is currently limited to YFV, validating our integrative approach in other flaviviruses and vector-host systems will be essential for the generalizability of our findings.

Materials and Methods

Resource Availability

The mass spectrometry proteomics data have been deposited to the ProteomeXchange Consortium (http://proteomecentral.proteomexchange.org) via the PRIDE partner repository[90]

486 with the dataset identifiers of PXD062491 for the YFV-Human AP-MS study and PXD062539 for
487 the YFV-*Aedes aegypti* AP-MS study. All code is available on GitHub
488 (https://github.com/shahlab247/YFV-human-aedes, https://github.com/jayoung/pamlWrapper).
489 Raw western blot, gel, and microscopy images are available upon request. The Foldseek protein
490 structure and NEEDLE protein sequence alignment output data are available on GitHub
491 (https://github.com/shahlab247/YFV-human-aedes) for both the forward (Human to *Aedes*
492 *aegypti*) and reverse (*Aedes aegypti* to Human) searches. Due to file size constraints, FATCAT
493 structural alignment data are available upon request. Numerical data associated with the
494 alignments for all three methods are available in Table S5. Plasmid maps for the codon-optimized
495 constructs are available upon request.

496 **Experimental models and tools**

497 *Cells:*

498 HEK293T (from Sam Diaz-Munoz), HeLa (from Luc Snyers), stably expressing Huh7-dCas9 and
499 Vero (ATCC) cells were cultured at 37°C with 5% CO_2 in Dulbecco's modified Eagle's medium
500 (DMEM) (Gibco) supplemented with 10% heat-inactivated fetal bovine serum (HI-FBS; Standard,
501 Gibco). Aag2-AF5 cells[55] (from Kevin Maringer) were cultured at 28°C with no CO_2 in Liebowitz's
502 L-15 media (Gibco) supplemented with 10% FBS (Performance Plus, Gibco), 10% tryptose
503 phosphate broth (Sigma Aldrich), 1X Non-essential amino acids, 1% penicillin-streptomycin
504 (Thomas Scientific), and 1% Amphotericin B (Gibco). All cell lines were tested monthly for
505 mycoplasma contamination using a MycoStrip test kit (Invivogen).

506 *Plasmid Constructs:*

507 Yellow fever virus isolate Asibi (GenBank accession: KF769016.1) protein-coding sequences
508 were codon-optimized (http://atgme.org) based on codon usage tables for *Homo sapiens* and
509 *Aedes aegypti* (Kazusa DNA Research Institute). Gene fragments were synthesized with Kozak
510 sequences (Twist Bioscience) for Gibson Assembly into pcDNA4_TO with a C-terminal 2xStrep

511 II affinity tag for expression in human cells and pAc with a C-terminal 2xStrep II affinity tag for
512 expression in Aag2-AF5 mosquito cells. HA-tagged RBBP6 domain deletions were previously
513 described (from Chris Basler)[77]. YFV NS5 truncations were designed based on known structural
514 elements and codons optimized for expression in human cells. Gene fragments were synthesized
515 (Twist Bioscience) and ligated into pcDNA4_TO cut with EcoRI and XhoI with C-terminal 2xStrep
516 II affinity tags by Gibson Assembly. Protein coding sequences are provided in Table S6.

517 *Viruses:*

518 YFV-17D (from Dr. Lark Coffey) stocks were propagated in Vero cells and monitored for CPE.
519 The supernatant was then harvested, and cell debris was removed by centrifugation (Eppendorf
520 centrifuge 5810 R, Rotor S-4-104, 211 g, 5 minutes, 4°C). Cleared supernatant was then
521 distributed into 1 mL aliquots and frozen at -80°C. Each aliquot was used only once to prevent
522 repetitive freeze-thaw cycles. Aliquots were titered by plaque assay (method below).

523 *Immunofluorescence microscopy:*

524 HeLa cells cultured on #1.5 coverslips were fixed with 4% paraformaldehyde (Fisher) for 15
525 minutes at room temperature. Cells were permeabilized with 0.1% Triton X-100 (Integra) for 10
526 minutes and blocked with 5% goat serum (Sigma) in PBS-Tween (0.1% Tween-20, Fisher).
527 Coverslips were incubated with primary antibodies overnight at 4°C. Coverslips were then washed
528 in PBS-Tween and incubated in secondary antibody at room temperature for 1 hour. Nuclei were
529 visualized with Hoechst (1:10000, Invitrogen). Confocal images were acquired using a Zeiss
530 Airyscan LSM980 with Axiocam using a 63x/NA1.40 oil immersion lens. Laser lines at 405, 488,
531 and 543nm were employed sequentially for each image using optics and detector stock settings
532 in the “Dye List” portion of the FluoView microscope-controlling software. All antibodies and
533 dilutions are listed in Table S7. Microscopy images were analyzed using ImageJ (Fiji) software[91].
534 Signal colocalization was quantified using Pearson’s correlation coefficient (R-value) determined

535 with the “JACoP” analysis tool imported into Fiji after setting regions of interest around entire
536 individual cells across at least 5 images.

537 *Western blotting:*

538 For whole cell lysates, cells were lysed in RIPA buffer (150 mM NaCl, 50 mM Tris Base, 1% Triton
539 X-100, 0.5% sodium deoxycholate) supplemented with protease inhibitors for 5 minutes at room
540 temperature. Otherwise, cells were lysed in IP buffer supplemented with Complete-EDTA-free
541 Protease Inhibitor Cocktail (Sigma Aldrich, USA). Cell lysate was incubated on ice for 30 minutes
542 prior to centrifugation (Eppendorf centrifuge 5424 R, Rotor FA-45-24-11, 13,500 g, 4ºC, 20 min).
543 When possible, the total protein concentration of each sample was normalized by BCA assay.
544 Protein samples (lysates or IP eluates) were resuspended in NuPAGE LDS sample buffer
545 supplemented with TCEP and boiled at 95ºC for 10 minutes. Samples were run on 7.5-12%
546 polyacrylamide gels for ~1 hour at 150 V and transferred to PVDF membranes (VWR) for 1 hour
547 at 330 mA on ice. Membranes were then blocked in 5% milk solution for 1 hour prior to overnight
548 incubation in primary antibodies (Table S7) at 4ºC. Membranes were washed 3x in Tris-buffered
549 saline with Tween-20 (TBS-T) (150 mM NaCl, 20 mM Tris Base, 0.1% Tween-20, Fisher) and
550 incubated with HRP-conjugated secondary antibodies in 5% milk for 1 hour at room temperature.
551 Membranes were again washed 3x in TBS-T and 1x in TBS (without Tween-20) prior to Pierce™
552 ECL activation (Fisher). Membranes were imaged using Amersham Imager 600 (GE).

553 *Plaque assay:*

554 Vero cells were seeded at 0.8×10^6 cells/well and grown in 6-well dishes overnight. Virus aliquots
555 were thawed on ice and subjected to 6-fold serial dilution. Media was removed from Vero cells,
556 and the monolayer was washed with 1xD-PBS. For YFV-17D, 900 µL of each virus dilution was
557 then added to the cells and incubated for 4 h at 37ºC. Virus was then removed, and cells were
558 overlayed with 2 mL of DMEM with 0.8% methylcellulose (Sigma), 1% FBS, 1%
559 penicillin/streptomycin, and incubated at 37ºC for 7 days. Cells were then fixed with 4%

560 formaldehyde and stained with 0.23% crystal violet solution (Fisher) for 30 minutes at room
561 temperature. The solution was then removed, and plaques were counted.

562 Generation of YFV proteomic networks

563 *Expression of viral proteins:*

564 For each affinity purification (AP) [YFV-Asibi protein constructs, empty vector, green fluorescent
565 protein (GFP)], $1x10^7$ human HEK293T or $3x10^7$ Aag2-AF5 mosquito cells were plated in 15 cm
566 cell culture dishes 24 hours prior to transfection. A total of 20 µg of plasmid DNA was transfected
567 in a 1 µg : 3 uL Polyjet (SignaGen) ratio for expression in HEK293T cells. Similarly, the same
568 mass of plasmid DNA was transfected in a 1 µg: 2 µL TransIT-Insect (Mirus Bio) ratio for
569 expression in Aag2-AF5 cells. Forty hours post-transfection, cells were gently washed in D-PBS
570 and dissociated with 10 mM EDTA in D-PBS. Cells were pelleted (250×*g*) at 4°C for 5 min, washed
571 in D-PBS, re-pelleted and lysed for 30 minutes on a rotator at 4°C in AP Buffer [50 mM Tris-HCl
572 pH 7.4, 150 mM NaCl, 1 mM EDTA, Pierce EDTA-free protease tablets (Thermo Scientific)]
573 supplemented with 0.5% Nonidet P 40 Substitute (NP40; Fluka Analytical). Subsequently, cell
574 debris was pelleted (4500×*g*) at 4°C for 20 minutes. A fraction of lysate was resolved on a hand-
575 cast 4→20% gradient SDS-PAGE gel to evaluate 2xStrep-tagged protein expression by Western
576 blotting. The remaining lysate was used for subsequent affinity purification.

577 *Strep-tag affinity purification and digest:*

578 Each cell lysate was combined with 100 µL of a 50% Strep-Tactin Sepharose bead (IBA
579 Lifesciences) slurry and incubated on a tube rotator for 2 hours at 4°C. After binding, beads were
580 washed in three times AP Buffer supplemented with 0.05% NP-40. For each wash, 1 mL of AP
581 buffer was added, tubes were inverted, and beads were pelleted (~500×*g*) at 4°C before removing
582 the supernatant. After a final wash in AP buffer without NP-40, 1/3 of the beads were transferred
583 to a fresh tube and eluted in 25 µL of 2.5 mM D-Desthiobiotin (IBA Lifesciences) by agitation
584 (1300 rpm) at room temperature. Like cell lysates, this eluate was resolved by SDS-PAGE and

585 protein expression was evaluated using both Western blotting and a Pierce Silver Stain (Thermo
586 Scientific). The remaining 2/3 of the beads were equilibrated in diminishing volumes (200 µL, 100
587 µL, 50 µL, 25 µL) of 50 mM Triethylammonium bicarbonate (TEAB) buffer (Thermo Scientific) at
588 4°C for 15 minutes on a tube rotator. At the final wash, 500 ng of Sequencing Grade Modified
589 Trypsin (Promega) was added to each sample. Beads were then incubated under agitation (1300
590 rpm) overnight at 37°C. The following morning, the digest supernatant was transferred to a new
591 protein LoBind tube (Eppendorf). Another 200 ng of trypsin was added to the beads, along with
592 40 µL of TEAB, and incubated for an additional 2 hours; this digest was then combined with the
593 previous extract.

594 *Mass spectrometry:*

595 Digested peptides were directly loaded onto an Evosep C18 tip and separated using the Evosep
596 One and the standard (human samples) or 100 spd High Organic method (mosquito samples)
597 (Evosep). Peptides were eluted and ionized using a Bruker Captive Spray emitter. A Bruker
598 TimsTof Pro 2 mass spectrometer running in diaPASEF mode was used for acquisition. The
599 acquisition scheme used for diaPASEF consisted of 6x3 50 m/z windows per PASEF scan. DIA
600 data was searched using Spectronaut 17 (Biognosys) against the human (UP000005640,
601 downloaded 6/15/2022) or *Aedes aegypti* (UP000008820, downloaded 2/10/2023) UniProt
602 proteomes, YFV protein sequences, and the standardized common contaminants database. The
603 Direct DIA workflow was used under default settings. Briefly, trypsin/P Specific was set for the
604 enzyme, allowing two missed cleavages. Fixed Modifications were set for Carbamidomethyl, and
605 variable modifications were set to Acetyl (Protein N-term) and Oxidation. For DIA search
606 identification, PSM and Protein Group FDR were set to 1%. A minimum of 2 peptides per protein
607 group were required for quantification. Raw intensity values were normalized to all mapped
608 peptides. Background detections were eliminated by excluding intensity values below the median
609 intensity value for each protein, and common contaminants were removed.

610 *PPI scoring and network visualization:*

611 We scored protein interactions with both Mass spectrometry interaction STatistics (MiST)[92] and
612 Significance Analysis of INTeractome Express (SAINTexpress)[93] platforms. For MiST scoring,
613 MS1 intensity values were treated as the quantifying feature, and weights were set to R= 0.35, S
614 = 0.57, and A = 0.08, in line with our previous flavivirus work[22]. Samples or baits were removed
615 from further analysis if they exhibited poor clustering or minimal/no detection of the bait itself in
616 the quality control step. Specificity exclusions were applied to baits with shared sequences (prM-
617 prME, NS2B-NS2B3, NS3-NS2B3) or those that exhibited high PPI overlap across previous
618 flavivirus-host proteomic studies (NS4A-NS4B and NS4A-NS2A). Each bait was compared to at
619 least 8 other baits for specificity scoring regardless of these exclusions. Concurrently, protein
620 interactions were also scored with SAINTexpress using the Galaxy APOSTL server
621 (http://apostl.moffitt.org/) under default parameters, with the GFP bait serving as the source of
622 control counts.

623 We mirrored a two-step filtering strategy for identifying high-confidence interactions
624 previously[64,94]. First, we selected all protein interactions with a MiST score > 0.67—as this
625 threshold was rigorous in past flavivirus-host proteomic studies[22]—and a SAINTexpress score >
626 0.95 and Bayesian false-discovery rate (BFDR) ≤ 0.05. We then identified if these proteins were
627 part of a curated human CORUM (4.0 release) protein complex[38], recovering any additional
628 complex members with a MiST score ≥ 0.6, a SAINTexpress score > 0.95 & BFDR ≤ 0.05, and
629 interacting with the same viral bait. All PPI networks were built in Cytoscape (v3.9.0) and
630 formatted with Affinity Designer. Prey proteins were annotated for GO: Biological Processes
631 (GO:BP), protein complexes were extracted from CORUM, and additional or overlapping
632 annotations were manually curated and grouped as needed.

633 ## Phenotypic screening and RBBP6 assays

634 *CRISPRi knockdown:*

635 Custom synthetic guide RNAs (gRNA) were acquired from Sigma and resuspended to 3 μM in
636 TE buffer (10 mM Tris Base, 1 mM EDTA, pH 8.0). For the knockdown experiment, 375 μL of
637 Opti-MEM (Life Technologies, USA), 5 μL of TransIT-CRISPR transfection reagent (Sigma, USA),
638 and 20 μL of gene-specific sgRNAs were combined and incubated at room temperature for 20
639 min, then added to the appropriate well of the 12-well plate. Approximately 0.5×10^5 cells were
640 plated to corresponding 12 well plates. After 72h, cells were washed with 1xPBS, lysed in RNA
641 lysis buffer (Thomas Scientific, USA), and the efficiency of gene knockdown was estimated by
642 qRT-PCR. Single-stranded cDNA was synthesized from total RNA using the iScript cDNA
643 Synthesis Kit (BioRad, USA) according to the manufacturer's recommendations. qPCR was
644 performed using SYBR Master mix (Invitrogen, USA). All qRT-PCR data were normalized to the
645 expression of the *GAPDH* gene. Expression fold changes were calculated by using the
646 ΔΔCt method. Genes with knockdown greater than 50% were prioritized for virus replication
647 assays. gRNA and qPCR primer sequences are available in Table S8.

648 *CRISPRi infection assay:*

649 Cells were infected with YFV-17D at the indicated MOI 72h after CRISPRi knockdown.
650 Supernatant aliquots were harvested at 0, 24, 48, and 72 hpi and frozen at –80ºC. The titration of
651 viral load in the infectious culture supernatants collected at different time points was conducted
652 by plaque assay in Vero cells in triplicates. For the CRISPRi screen, robust *z*-scores were
653 calculated for log-transformed titers measured at 48 hpi. The complete screening results can be
654 found in Table S2.

655 *Endogenous RBBP6 immunoprecipitation:*

656 At 48 hours post-infection, mock or YFV-17D-infected Huh7 cells (MOI of 1) were collected,
657 washed twice with ice-cold PBS and lysed with immunoprecipitation buffer (50 mM Tris-HCl pH

658 7.5, 140 mM NaCl, 1.5 mM $MgCl_2$, 0.5% NP-40) supplemented with Complete-EDTA-free
659 Protease Inhibitor Cocktail. Cell lysates were incubated for 30 min on ice. After clearing lysates
660 by centrifugation at 1000 x g for 10 min at 4°C, they were treated or not with RNaseA (Thermo
661 Fisher Scientific, USA) for another 30 min. Following this, 25 µL of lysates (treated and not treated
662 with RNaseA) were preserved as protein Input while another aliquot (25 µL) was used to perform
663 IP. A total of 25 µl of Protein A Mag Sepharose beads (Cytiva, USA) had been equilibrated with
664 cold washing buffer (50 mM tris, 150 mM NaCl pH 7.5) and incubated overnight with agitation at
665 4°C with anti-RBBP6 (Origene, USA) and negative control rabbit IgG (Santa Cruz Biotechnology,
666 USA) antibodies. Following this, the cell lysates were added to the beads and incubated for 1 h
667 on ice. The supernatants were removed, and beads were washed 3 times with 500 µl washing
668 buffer (50 mM tris, 150 mM NaCl pH 7.5). After the last washing step, beads were resuspended
669 in 50 µl of western blot loading buffer and boiled at 95°C for 10 min. Obtained samples (IPs and
670 Inputs) were analyzed by Western blotting.

671 *YFV replicon assay:*

672 YF-Rluc-2A-WT expressing plasmid (gift of Richard Kuhn[50]) (10 µg) was linearized using XhoI
673 enzyme (NEB, United States) prior to *in vitro* transcription. The linearized DNA was purified using
674 Gel and PCR Clean-up, NucleoSpin (Macherey-Nagel, USA). The capped RNA transcripts were
675 synthesized using an SP6 mMessage mMachine kit (Invitrogen, USA), and the obtained RNA was
676 precipitated with Lithium Chloride following the manufacturer's instructions. Huh7-dCas cells were
677 first transfected with ncgRNA, RBBP6 gRNA1, and RBBP6 gRNA2 and 48h later transfected with
678 the obtained RNA transcripts (5 µg/per reaction) using Lipofectamine 2000 (Invitrogen, USA).
679 Briefly, transfection mixtures were incubated at room temperature for 15 min, added to the cells,
680 and then incubated for 4–6 h at 37°C. After incubation, 1mL of complete growth medium was
681 added to each well. The cells were lysed at 0, 3, 6, 12, 24, and 48 h post-transfection and stored
682 at −20°C. All the measurements of luciferase activity were performed by *Renilla* luciferase assay

683 kit according to manufacturer instructions (Promega Corporation, USA) and using a Spectramax
684 m2 plate reader (Molecular Devices, USA).

685 Identification and conservation analysis of interologs

686 *Interolog mapping of mosquito proteins:*

687 To appropriately compare human and mosquito PPI networks, we mapped *Aedes aegypti*
688 mosquito proteins to human orthologs. We leveraged a multi-stepped approach to maximize
689 ortholog identification. In brief, we extracted all possible ortholog mappings from the InParanoid
690 8 database[60] between *Homo sapiens* and *Aedes aegypti*, mapping a majority of mosquito
691 proteins. Some annotations were additionally mapped using OrthoDB[95]. Each of these
692 annotations is provided in the supplemental network file (Table S4B).

693 *Identification of interologs by AlphaFold2 and Foldseek:*

694 To enhance interolog identification, we extracted both *A. aegypti* and human proteomes from the
695 AlphaFold EMBL-EBI database (https://alphafold.ebi.ac.uk/). The human proteome is readily
696 available for download, while the *A. aegypti* proteome must be downloaded from a separate
697 repository available through the same website. In total, there were 23,391 and 30,561 structures
698 for each organism, respectively. These numbers exceed the actual quantity of annotated and
699 predicted proteins for each organism because larger proteins are split into sections to make
700 predictions via AlphaFold tractable. We first performed an all-versus-all comparison of the two
701 proteomes using Foldseek to identify potential structural homologs for every protein: human to *A.*
702 *aegypti* (forward search) and *A. aegypti* to human (reverse search). Foldseek performs a rigid
703 structural alignment with a 3D alphabet approach that allows for rapid searches against entire
704 proteomes on local computer systems. Foldseek can identify hundreds of similar structures for a
705 single query with varying levels of confidence structure (represented as an e-value), so we limited
706 results to any structure with an e-value below 1e-10. We then took the intersection of the two
707 datasets for an aggregate of structural homolog pairs between the forward and reverse search of

708 the human and *A. aegypti* proteomes. From this list, the 3 pairs with the smallest e-values were
709 retained for further analysis. We added homologs identified by inParanoid8 to alleviate bias
710 toward highly structured proteins that could be predicted confidently by AlphaFold. We performed
711 flexible structural alignments using FATCAT for all filtered structural homolog pairs. Duplicate
712 pairs generated from proteins with multiple sectioned structures were removed using the p-value
713 output by FATCAT, resulting in a final 32,749 structural homolog pairs. These pairs were
714 compared to both the YFV and DENV HC-PPI datasets. If either a human or *A. aegypti* protein
715 appeared as a HC-PPI with a viral bait, we classified the pair as a HC-PPI. If both the human and
716 *A. aegypti* proteins in a structural homolog pair appeared as a HC-PPI for the same viral bait, we
717 classified them as structural interologs.

718 *Sequence similarity analysis of interologs:*

719 For the 32,749 structural homolog pairs, we performed sequence alignments using the EMBOSS
720 Needle algorithm. We maintained the same categorizations for each pair plotted.

721 Positive selection analysis:

722 To examine the evolutionary selective pressures acting on *RBBP6* and 17 unique high-confidence
723 interologs in primates, we first selected the human splice isoform with the longest ORF for each
724 gene. We used each ORF as query in a blastn[96] search of NCBI's nt database, restricting hits to
725 simian primates. For each non-human primate species, we collected the hit with the highest bit
726 score and obtained its ORF sequence. We generated an in-frame alignment using the MACSE[97]
727 algorithm and made manual adjustments to fix likely gene prediction errors and alignment
728 ambiguities. We then estimated a phylogeny from each alignment using phyml[98], with the GTR
729 nucleotide substitution model, four rate categories, and estimating the proportion of invariable
730 sites.

731 We used the resulting alignments and trees as inputs to the PAML[99] algorithm (codon model 2,
732 starting omega 0.4), comparing the likelihoods of evolutionary models that allow positive selection

733 at a subset of sites (models 8 and 2) with nested models that allow only sites with purifying or
734 neutral selection (models 7, 8a and 1). Results are shown in Table S3. Four genes had a p-value
735 ≤ 0.05 in our preferred test (model 8 versus 8a); however, after correction for multiple testing
736 using the Benjamini and Hochberg (BH) method[100], only one (*MRPS9*) remained significant.
737 We also ran the GARD algorithm[101] to examine alignments for recombination and gene
738 conversion, which can cause false positives in evolutionary analysis. One of the genes that
739 showed evidence of positive selection (*NOP53*) also showed evidence of recombination. We
740 reran PAML on each GARD-identified segment separately, finding that the signal of positive
741 selection remained for segment 1. However, close inspection of the *NOP53* results revealed only
742 a single amino acid position (codon 6) with a high likelihood of positive selection (> 90% BEB
743 posterior probability) - this codon overlaps a CpG dinucleotide in a very CpG-rich region at the 5'
744 end of the gene. Methylated CpG sites are known to mutate at much higher rates than other
745 sequences[102], a phenomenon that PAML (like other algorithms to detect selective pressure) does
746 not account for. While it is possible that positive selection drove changes at this residue, it seems
747 more likely that the number of changes observed at this site reflects its hypermutability. As a
748 conservative approach to mitigate the impact of CpG hypermutation, we masked alignments to
749 remove any codon that overlapped a CpG dinucleotide in any species in the alignment and re-ran
750 PAML. Statistical support for positive selection disappeared for *NOP53* but remained for *MRPS9*,
751 *DDX21*, and *MRPS31*. We also checked whether the signature of positive selection in these four
752 genes was robust to the use of alternative starting parameters (codon models 2 or 3, starting
753 omega 0.4 or 3, model 8 versus 8a p ≤ 0.05). For *MRPS9*, *DDX21*, and *MRPS31*, all four starting
754 parameter combinations yielded evidence of positive selection; *NOP53* gave more equivocal
755 results, where two of the four-parameter combinations had p ≤ 0.022, and the other two had p =
756 0.059. Full positive selection results are available in Table S3.

757 ## Integrative analysis of protein interactions

758 *Network similarity metrics:*

759 When comparing the overlapping bait-prey data between various datasets, the relevant data were
760 reformatted into a contingency table. A Fisher's exact test was performed to assess the statistical
761 significance of the overlap using the GeneOverlap R package (v1.32.0). Venn diagrams showing
762 the degree of overlap were created with the BioVenn R package (v1.1.3).

763 *Enrichment analyses:*

764 All gene enrichment analyses were conducted with the R package gprofiler2 (0.2.1). Typically, we
765 separated genes into lists by viral bait and/or hierarchal cluster prior to enrichment. Using the
766 "gost" function, we tested for functional enrichment across Gene Ontology (GO), Reactome
767 Pathways, and CORUM databases. Statistical significance was calculated with a hypergeometric
768 test, correcting for false discovery rate (FDR) using the Bonferroni method. Enrichment analyses
769 for both human and mosquito data were performed using *Homo sapiens* databases against all
770 annotated genes, meaning mosquito proteins without an annotated ortholog were excluded from
771 these analyses.

772 *Hierarchal clustering of protein interactions:*

773 We performed hierarchal clustering on interactions for viral bait proteins shared across all five
774 viral bait datasets and that met their respective MiST cutoffs in at least one of the datasets.
775 Clustering was performed on MiST scores for each virus-host interaction using the "hclust"
776 function and "ward.D2" method of the base R package stats. We optimized the number of clusters
777 by applying k-means clustering and selecting a hierarchal cutoff that produced the equivalent
778 number of clusters. Enrichment analyses were conducted by both cluster and viral protein, as
779 described previously. Thus, we could extract unique or shared enrichment categories ($p < 0.05$)
780 for a particular bait and cluster. Clustering was visualized with the R package pheatmap (v1.0.12).

781 *DIS analysis and scoring:*

782 Differential interaction scores (DIS) were calculated for the same subset of data used for
783 hierarchal clustering by finding the difference in MiST scores between two viruses for a particular
784 bait-prey interaction. We excluded cases where both MiST scores were 0. To ascertain the level
785 of correlation across DIS, Pearson's correlations were calculated based on the distribution of DIS
786 between two particular comparisons. Distributions were visualized with the R package ggplot2
787 (v3.4.1).

788 *Enrichment network visualization:*

789 To simplify enrichment data for visualization, we isolated enriched terms between 1 and 2000
790 genes and eliminated redundancy by collapsing terms with greater than 50% similarity, retaining
791 the term with the lowest adjusted p-value. Cytoscape (v3.9.0)[103] was used to plot these as
792 networks, and the "geom_tile" function of ggplot2 created heatmaps of relevant baits/clusters.

793 Conservation analysis of PPIs by viral bait using protein sequence and 794 structure

795 *HC-PPI conservation analysis and MiST profile correlations:*

796 MiST scores for YFV, DENV, WNV, and ZIKV were compiled by viral bait, excluding any entries
797 that were not detected by MS in all four datasets. Pairwise Pearson's correlation coefficients were
798 calculated in R. The union of HC-PPIs for YFV, DENV, WNV, and ZIKV was compiled by viral
799 bait. For each PPI, a relative conservation was calculated based on the fraction of datasets that
800 PPI was conserved. This was summed over the entire union for each viral bait. Since each viral
801 bait had a different number of HC-PPIs, ranging from 20 to 74, this was normalized to the total
802 number of HC-PPIs for that bait.

803 *Viral protein sequence identity calculations and visualization:*

804 Amino acid sequences for flavivirus proteins from YFV, WNV, DENV, and ZIKV were collected
805 from sequences used in published proteomics studies[22,23] or this study. Sequence identity was

806 determined using the T-Coffee alignment algorithm within SnapGene (v4.3.11)
807 (www.snapgene.com). Protein structures were predicted using AlphaFold2 and visualized using
808 UCSF ChimeraX (v1.9)[104]. YFV Capsid and NS5 structures were colored based on the four
809 viruses, ranging from 25% (1 out of 4) to 100% (4 out of 4) amino acid identity. Solvent-accessible
810 surface area (SASA) calculations were performed using UCSF ChimeraX (v1.9).

811 *Statistical analysis:*

812 Simple linear regression was applied to data when indicated to calculate Pearson's correlation
813 coefficients. P-values of correlation coefficients were calculated by bootstrapping the linear
814 regression. The indicated data was shuffled, and the correlation coefficient was calculated. This
815 was repeated 100,000 times to create a distribution of correlation coefficients. The percentage of
816 randomly generated correlation coefficients greater (for positive correlation coefficients) or less
817 (for negative correlation coefficients) than the true correlation coefficient was taken as the P-
818 value.

819 Supplementary Files

820 Table S7: Antibodies

Antibody	Host Species	Dilution Used	Supplier (Catalog #)	RRID
GAPDH	Mouse	1:1000 (WB)	Fisher (PIMA515738)	AB_2537652
FLAG-M2	Mouse	1:200 (IF), 1:1000 (WB)	MilliporeSigma (F1804)	AB_262044
Strep	Mouse	1:1000 (WB), 1:500 (IF)	Qiagen (34850)	AB_2810987
HA	Mouse	1:1000 (WB), 1:200 (IF)	MilliporeSigma (H3663)	AB_262051
TOMM20	Rabbit	1:250 (IF)	ThomasScientific (11802-1-AP)	AB_2207530
Calnexin	Rabbit	1:250 (IF)	Proteintech (10427-2-AP)	AB_2069033
RBBP6	Rabbit	1:1000 (WB)	ThermoFisher (PA5-23054)	AB_11152136
YFV NS5	Rabbit	1:1000 (WB)	GeneTex (GTX134141)	AB_2887231
GRASP65	Rabbit	1:250 (IF)	From Dr. Nevan Krogan	N/A
Anti-Mouse IgG-HRP	Rabbit	1:5000 (WB)	SouthernBiotech (6170-05)	AB_2796243
Anti-Rabbit IgG-HRP	Goat	1:5000 (WB)	SouthernBiotech (4030-05)	AB_2687483
Anti-Mouse AlexaFlour-488	Goat	1:1000 (IF)	Invitrogen (A28175)	AB_2536161

Anti-Mouse AlexaFlour-555	Goat	1:1000 (IF)	Invitrogen (A21422)	AB_2535844
Anti-Rabbit AlexaFlour-488	Goat	1:1000 (IF)	Invitrogen (A11008)	AB_143165
Anti-Rabbit AlexaFlour-555	Goat	1:1000 (IF)	Invitrogen (A27039)	AB_2536100

821

822 **Table S8: Oligonucleotides**

Oligo Name	Sequence (5' > 3')
pcDNA / pAc5 Upstream	CGAGCTCGGATCCACTAGTC
pcDNA / pAc5 Downstream	GTTTAAACGGGCCCCTTCTC
Negative CRISPRi gRNA #1	CGCGAUAGCGCGAAUAUAUU
Negative CRISPRi gRNA #2	GCGCGAUAGCGCGAAUAUAC
ATRX CRISPRi gRNA #1	AAUUCCGAGUUUCGAGCGA
ATRX CRISPRi gRNA #2	GGUGUAGUCUUUACACGUG
DAXX CRISPRi gRNA #1	CUGGGAUGCCAUUCCACUA
DAXX CRISPRi gRNA #2	GAUCUGGAACAGAUGCAGG
DDX10 CRISPRi gRNA #1	UUCCACUUCGUCAUUGGUG
DDX10 CRISPRi gRNA #2	AGCCUUAUAUCGUCUGCAA
XRCC6 CRISPRi gRNA #1	UCCUCUGGGUACACGAACA
XRCC6 CRISPRi gRNA #2	GAGACCUCUUGGUAUCGCU
ILF2 CRISPRi gRNA #1	CUCGAACCAGCGGGCAUGU
ILF2 CRISPRi gRNA #2	CAAAUUGAAGAAGUUCGAC
RBBP6 CRISPRi gRNA #1	GGAGGGACACUAUACCCAG
RBBP6 CRISPRi gRNA #2	GUGAUCUGCAGGUCGCAGU
TMPO CRISPRi gRNA #1	CCGCCGGCACCAACAGCAA
TMPO CRISPRi gRNA #2	CUUUGCGCUGCUCCCCGGC
ZRANB2 CRISPRi gRNA #1	CCUAGACCUUGAACUUGAG
ZRANB2 CRISPRi gRNA #2	AUUAGCACUAAAUAGGCCU
STUB1 CRISPRi gRNA #1	AAUCGCGAAGAAGAAGCGC
STUB1 CRISPRi gRNA #2	GAGUGCCAGCGAAACCACG
KRR1 CRISPRi gRNA #1	AGUCAUGCUGCCUUCGAUC
KRR1 CRISPRi gRNA #2	CUGGUUCCUUCCAACCAUC
ZC3H4 CRISPRi gRNA #1	GGUGUGGUACAGCUUACAC
ZC3H4 CRISPRi gRNA #2	CCCUCCUUGUUUGAGAUCG
GNL3 CRISPRi gRNA #1	ACCUCUAGGACAACAUCGG
GNL3 CRISPRi gRNA #2	GCGCAGAGGAGGAAUUAAG
PRPF19 CRISPRi gRNA #1	CUCAUCGAGAAGUACAUUG
PRPF19 CRISPRi gRNA #2	AAUCCUGAUAGUGGCAUCG
TFB1M CRISPRi gRNA #1	GUGGAGUUGAAACACUAAA
TFB1M CRISPRi gRNA #2	CUCGAAUCGUGGGCAACGG
ZFR CRISPRi gRNA #1	AAUAGGCUACACCCGAAGC
ZFR CRISPRi gRNA #2	AUCGCCGCCGAAUGCCAGA

SARAF CRISPRi gRNA #1	GACUACAAACGCGAUCCCA
SARAF CRISPRi gRNA #2	GAUACUCAGAGUACGGUGG
EIF4ENIF1 CRISPRi gRNA #1	GAAAGAGUUGGAUACAGAC
EIF4ENIF1 CRISPRi gRNA #2	AACCACCUACUGAACCGAC
DDX54 CRISPRi gRNA #1	CGAGGAGAAGCGCGCACGG
DDX54 CRISPRi gRNA #2	UCAGAGCGGGAGCCGAAGU
CACTIN CRISPRi gRNA #1	CUGGGCGUUAUCAGCAACG
CACTIN CRISPRi gRNA #2	UUUGGCGAGAUUGAUCUUG
GAPDH qPCR Forward	ACATCGCTCAGACACCATG
GAPDH qPCR Reverse	TGTAGTTGAGGTCAATGAAGGG
RBBP6 qPCR Forward	AGATTCAAAAGGAGCGTAGGC
RBBP6 qPCR Reverse	TCGAGAATAAGAGCGTGAACG
ZRANB2 qPCR Forward	TCTTCATCACGCTCATCCTC
ZRANB2 qPCR Reverse	AGATCTCGAACGTTCTCTGG
CACTIN qPCR Forward	TACACCAACACCGACAACCC
CACTIN qPCR Reverse	TTCAGCTCCTTCTCCTCCAG
ZC3H4 qPCR Forward	CGCAAGTACAGAGAGTACAG
ZC3H4 qPCR Reverse	CCATAACTCTTGCTGTCCAT
SARAF qPCR Forward	GTTTTGGCAGTGCTTTTACA
SARAF qPCR Reverse	ACGAGTCTGAGAAGGGTGTT
TFB1M qPCR Forward	CGTAGTCGCCTCTCTGTTATGG
TFB1M qPCR Reverse	GCTGCTCTATCTTGGGCTGTATC
ZFR qPCR Forward	AGACAGAGCTTTGAAAGGAG
ZFR qPCR Reverse	CAGCAAAACAAGGTTGACAT
DAXX qPCR Forward	GTTCTGAGAATTGCGGCGAG
DAXX qPCR Reverse	GGTGGCCATAGGGGATCAAA
ATRX qPCR Forward	AGAAACAAGTTCTCCTCCAC
ATRX qPCR Reverse	CTTCCTTGCTGTTTTCCATC
GNL3 qPCR Forward	AAGGTGCTGCCAAACTGC
GNL3 qPCR Reverse	CTCCTGCTTCCTTTCTTTCC
DDX10 qPCR Forward	TTGAGGTTCTCCGAAAAGTAGG
DDX10 qPCR Reverse	ACATTTGGAGGTCGGTAGCAT
PRPF19 qPCR Forward	ATGGTTACTACCTGGCTACAGCGG
PRPF19 qPCR Reverse	TGCCTGTTGAAGCGATGAACTTGG
TMPO qPCR Forward	TGCTCGCCTCCTGCCTGTAG
TMPO qPCR Reverse	GACACAAAGCCAAGCCAGACC
EIF4ENIF1 qPCR Forward	GGTTTCACACCAGGACCACA
EIF4ENIF1 qPCR Reverse	CATCTGGGCTGTGATGGGG
XRCC6 qPCR Forward	AGTCATATTACAAAACCGAGGGC
XRCC6 qPCR Reverse	CCTTGGAGGCATCAACCAAAAA
DDX54 qPCR Forward	AGGAAGAAGAAAGGGCTCCG
DDX54 qPCR Reverse	GTCTTCCAGGTCCCAGCTTC

STUB1 qPCR Forward	AGC AGG GCA ATC GTC TGT TC
STUB1 qPCR Reverse	CAA GGC CCG GTT GGT GTA ATA
ILF2 qPCR Forward	TCTGGTTTAGTGTGAAATGGCCT
ILF2 qPCR Reverse	AGCCAGGTCCTGATTCCTCT
YFV NS5 qPCR Forward	TCCGAAGTCATGCAGCCATT
YFV NS5 qPCR Reverse	GGAAAAGAGAGAAGAAGCTGTC

Acknowledgements

We thank members of the Shah Lab for constructive feedback and rewarding discussions. Funding for this work was provided by NIH R21AI168716, NIH R01AI170857, and the Laboratory Directed Research and Development Program at Sandia National Laboratories under Project 233120 to P.S.S. Funding to the proteomics core was provided by Dr. Neil Hunter and the Howard Hughes Medical Institute. Work in the Malik lab was supported by NIH U54AI170792 (PI: Nevan Krogan); H.S.M. is an Investigator at the Howard Hughes Medical Institute. The Zeiss 980 confocal microscope used in this study was purchased using NIH Shared Instrumentation Grant S10OD026702. We thank Thomas Wilkop of the MCB Light Microscopy Imaging Facility, which is a UC Davis Campus Core Research Facility, for assistance using this microscope.

Author Contributions

P.S.S. and M.W.K. conceived the project and designed experiments, with input from L.C., C. L. S. S., H.S.M., J.M.Y., and T.B.. M.W.K. performed affinity purification and designed computational pipeline for scoring YFV proteomics and subsequent comparative analyses with contributions from C.L.S.S. and P.S.S.. L.C. and C.J.F. performed CRISPRi knockdowns and associated virus assays. L.C. performed assays related to RBBP6. M.W.K., L.C., A.T.F., V.P., and C.J.F. performed Western blotting analyses. A.T.F. and M.W.K. conducted molecular cloning, performed immunostaining and microscopy. C.L.S.S., T.B., J.M.Y., and P.S.S. performed computational structure and evolution studies. M.W.K., C.L.S.S, and P.S.S. performed data visualization. P.S.S. and H.S.M. supervised the research. P.S.S. and H.S.M. acquired funding. M.W.K., H.S.M, and P.S.S. wrote The Manuscript. L.C., C.L.S.S., A.T.F., T.B., and J.M.Y. edited The Manuscript.

Declaration of Interests

All authors report no competing interests.

Figures

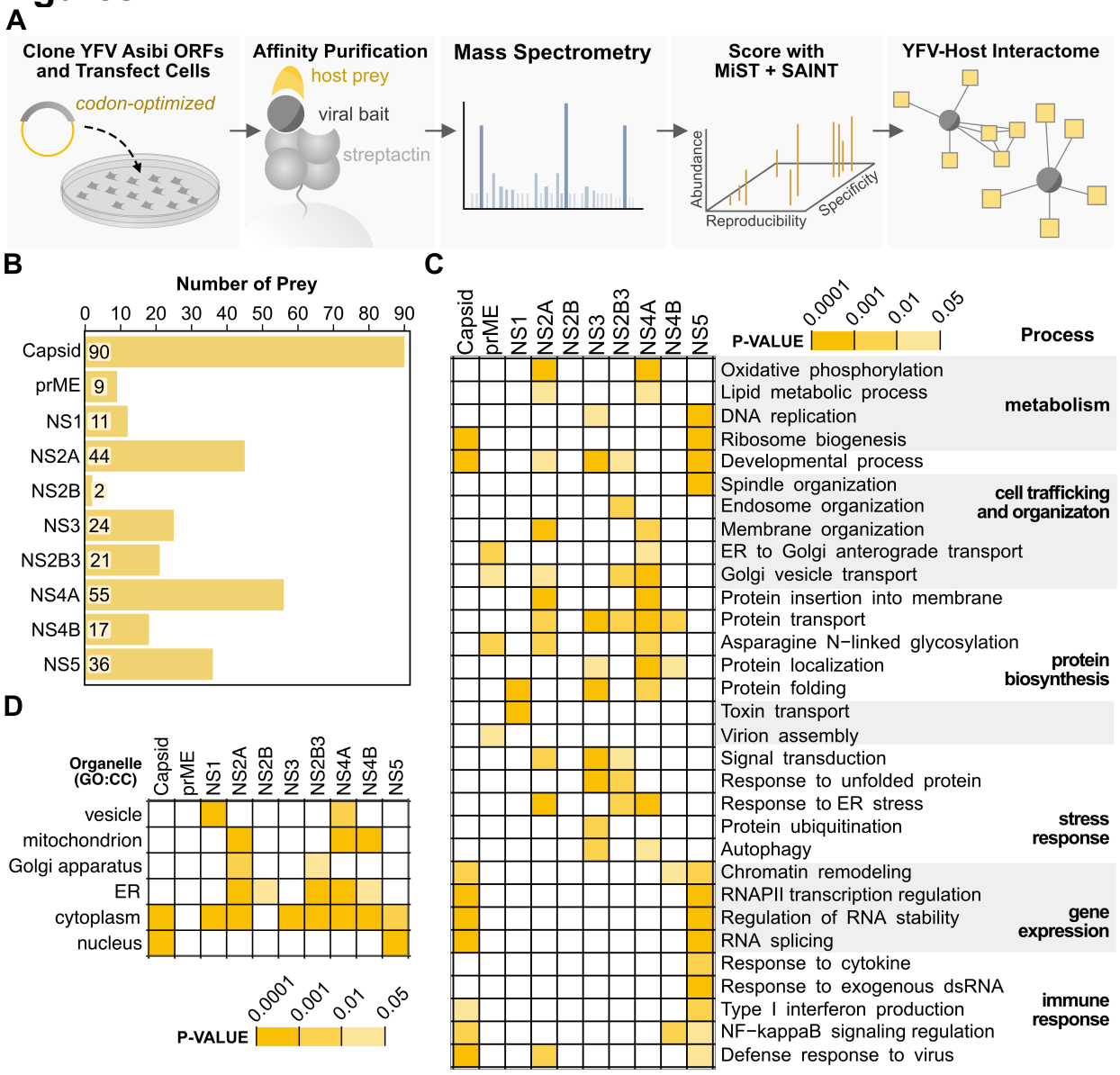

Figure 1. YFV-human proteomics identifies virus-host PPIs related to flavivirus biology.

(A) Schematic representation of experimental AP-MS pipeline and proteomic scoring.

(B) Virus-host interactions were scored with both MiST and SAINT to produce the plotted number of HC-PPIs per bait.

(C-D) Enrichment analysis was performed on the set of HC-PPIs for each viral bait. The heatmaps summarize the degree of enrichment (adjusted p-value < 0.05) for (C) GO: Biological Processes and Reactome pathways relevant to flavivirus replication, and (D) GO:cellular

855 compartment. The full enrichment results are available in Table S1. Viral baits are ordered
856 according to their position in the viral polyprotein.

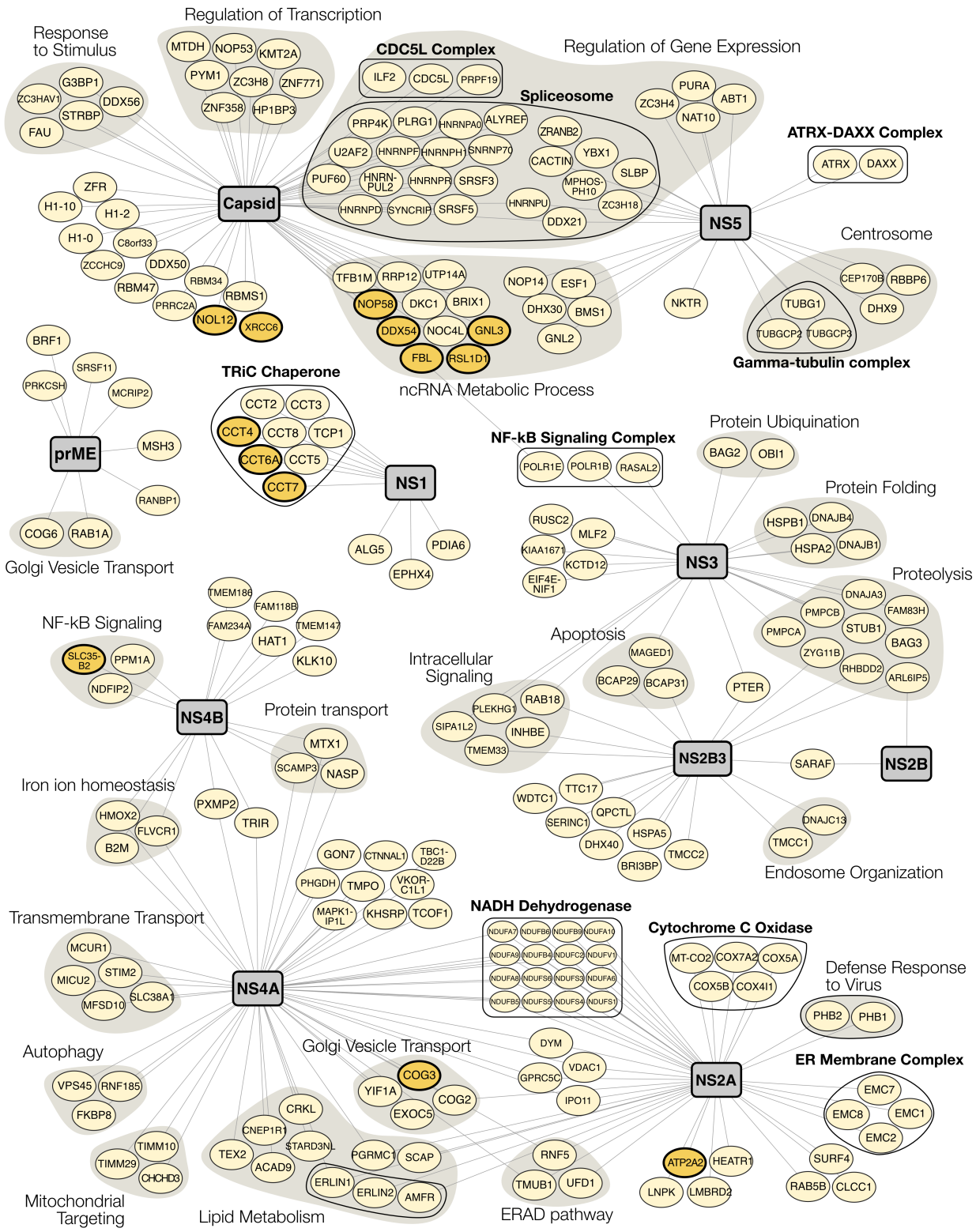
Response to Stimulus
G3BP1
ZC3HAV1
DDX56
STRBP
FAU
Regulation of Transcription
MTDH
NOP53
KMT2A
PYM1
ZC3H8
ZNF771
ZNF358
HP1BP3
CDC5L Complex
ILF2
CDC5L
PRPF19
Regulation of Gene Expression
Spliceosome
PRP4K
PLRG1
HNRNPA0
ALYREF
ZRANB2
U2AF2
HNRNPF
HNRNPH1
SNRNP70
CACTIN
YBX1
PUF60
HNRN-PUL2
HNRNPR
SRSF3
MPHOS-PH10
SLBP
HNRNPD
SYNCRIP
SRSF5
HNRNPU
ZC3H18
DDX21
ZC3H4
PURA
ABT1
NAT10
ATRX-DAXX Complex
ATRX
DAXX
Capsid
NS5
ZFR
H1-10
H1-2
H1-0
C8orf33
ZCCHC9
DDX50
RBM47
RBM34
RBMS1
PRRC2A
NOL12
XRCC6
TFB1M
RRP12
UTP14A
NOP58
DKC1
BRIX1
DDX54
NOC4L
GNL3
FBL
RSL1D1
NOP14
ESF1
DHX30
BMS1
GNL2
NKTR
Centrosome
CEP170B
RBBP6
TUBG1
DHX9
TUBGCP2
TUBGCP3
Gamma-tubulin complex
ncRNA Metabolic Process
BRF1
SRSF11
PRKCSH
MCRIP2
prME
MSH3
RANBP1
COG6
RAB1A
Golgi Vesicle Transport
TRiC Chaperone
CCT2
CCT3
CCT4
CCT8
TCP1
CCT6A
CCT5
CCT7
NS1
ALG5
PDIA6
EPHX4
NF-kB Signaling Complex
POLR1E
POLR1B
RASAL2
Protein Ubiquination
BAG2
OBI1
Protein Folding
HSPB1
DNAJB4
HSPA2
DNAJB1
RUSC2
MLF2
KIAA1671
KCTD12
EIF4E-NIF1
NS3
Proteolysis
DNAJA3
PMPCB
FAM83H
PMPCA
STUB1
BAG3
ZYG11B
RHBDD2
ARL6IP5
PTER
TMEM186
FAM118B
FAM234A
TMEM147
HAT1
KLK10
NF-kB Signaling
SLC35-B2
PPM1A
NDFIP2
NS4B
Apoptosis
MAGED1
BCAP29
BCAP31
Intracellular Signaling
RAB18
PLEKHG1
SIPA1L2
INHBE
TMEM33
NS2B3
SARAF
NS2B
Protein transport
MTX1
SCAMP3
NASP
Iron ion homeostasis
HMOX2
FLVCR1
B2M
PXMP2
TRIR
WDTC1
TTC17
QPCTL
SERINC1
HSPA5
DHX40
TMCC2
BRI3BP
DNAJC13
TMCC1
Endosome Organization
GON7
CTNNAL1
TBC1-D22B
PHGDH
TMPO
VKOR-C1L1
MAPK1-IP1L
KHSRP
TCOF1
NADH Dehydrogenase
NDUFA7
NDUFB6
NDUFB9
NDUFA10
NDUFA9
NDUFB4
NDUFC2
NDUFV1
NDUFA8
NDUFS6
NDUFS3
NDUFA6
NDUFB9
NDUFS5
NDUFS4
NDUFS1
Cytochrome C Oxidase
MT-CO2
COX7A2
COX5A
COX5B
COX4I1
Defense Response to Virus
PHB2
PHB1
Transmembrane Transport
MCUR1
STIM2
MICU2
SLC38A1
MFSD10
NS4A
Autophagy
VPS45
RNF185
FKBP8
Golgi Vesicle Transport
COG3
YIF1A
COG2
EXOC5
DYM
VDAC1
GPRC5C
IPO11
NS2A
ER Membrane Complex
EMC7
EMC8
EMC1
EMC2
TIMM10
TIMM29
CHCHD3
CRKL
CNEP1R1
TEX2
STARD3NL
ACAD9
PGRMC1
SCAP
ERLIN1
ERLIN2
AMFR
RNF5
TMUB1
UFD1
ATP2A2
HEATR1
LNPK
LMBRD2
SURF4
RAB5B
CLCC1
Mitochondrial Targeting
Lipid Metabolism
ERAD pathway
YFV protein (10)
Human protein (235)
GO:BP
YFV-human PPI (265)
YFV host-dependency factor (13)
CORUM complex

857

858 **Figure 2. YFV-human PPI network.**

859 YFV-Human HC-PPIs were identified after a tiered scoring approach using both MiST (M > 0.67
860 | M > 0.60 & protein complex member) and SAINT (score > 0.95 & BFDR ≤ 0.05). Viral baits (grey
861 rectangles) are mapped to human proteins (light yellow ovals). Human proteins are annotated as
862 host-dependency factors from a contemporary YFV CRISPR screen (gold with bolded borders).
863 Additionally, human proteins were grouped by GO:BP (grey underlay) and CORUM protein
864 complex (black outline). Full scoring results are available in Table S1. Ribosomal proteins (42)
865 were not included for visual clarity.

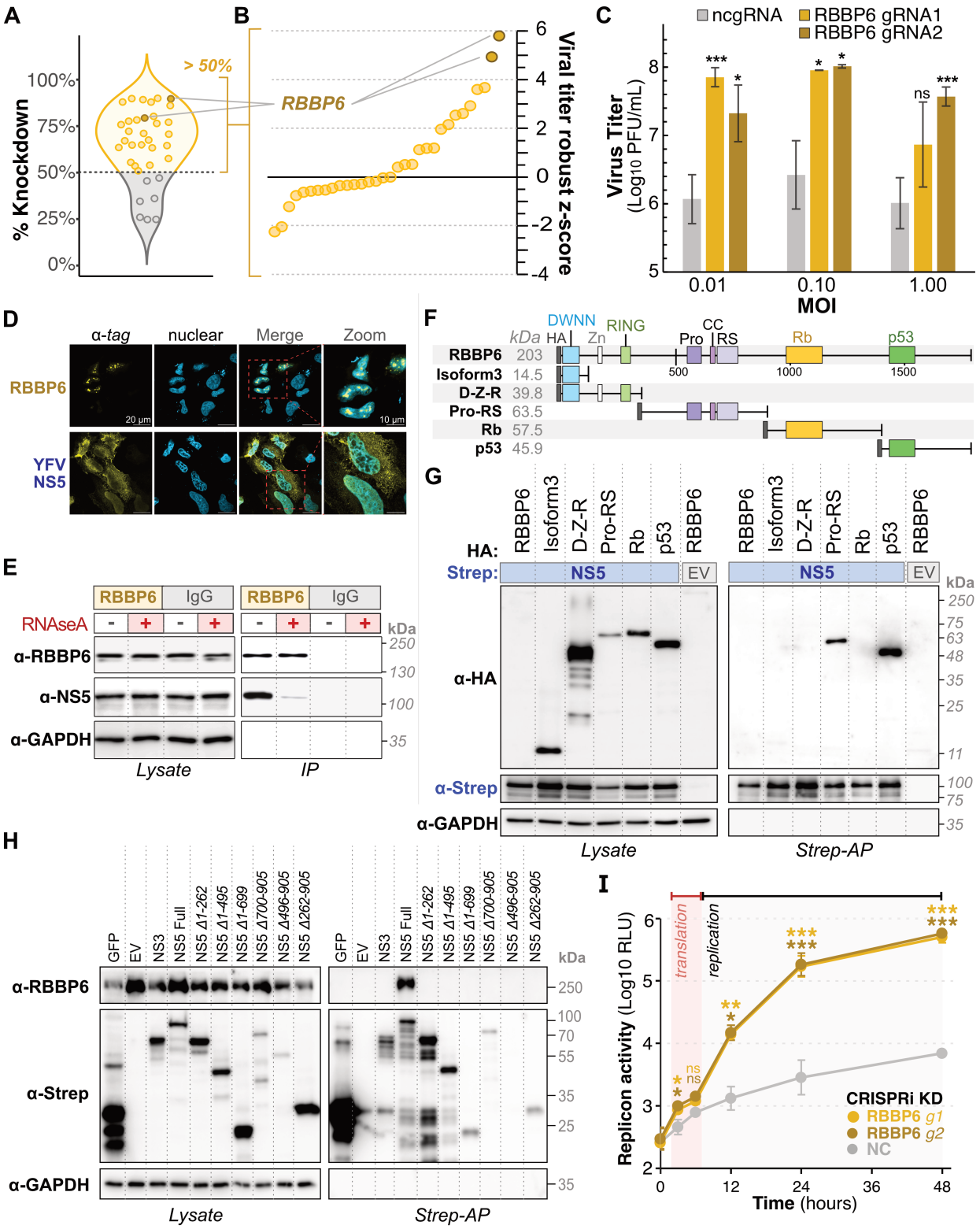

Figure 3. RBBP6 inhibits YFV genome replication through an RNA-dependent interaction with full-length NS5.

869 (A) Violin plot showing the percent knockdown efficiency of all tested gRNAs in the CRISPRi
870 screen. gRNAs achieving achieved >50% knockdown are shown in yellow. RBBP6-targeting
871 gRNAs are shown in bronze.

872 (B) Robust Z-score distribution of viral titers from the CRISPRi screen for gRNAs achieving >50%
873 knockdown (panel A, yellow), identifying RBBP6 as a top restriction factor (bronze). Full results
874 are available in Table S2.

875 (C) YFV-17D replication in Huh7 cells with RBBP6 knockdown. Plaque assay quantification of
876 viral titers at 48 hours post-infection (hpi) across a range of multiplicities of infection (MOI = 0.01,
877 0.10, 1.00). Data represent mean ± SD of three biological replicates, with $p < 0.005$ (***), $p < 0.01$
878 (**), and $p < 0.05$ (*) by one-sided t-test.

879 (D) Confocal immunofluorescence microscopy of RBBP6 and YFV NS5 in transfected HeLa cells.
880 2xStrep-tag for NS5 and HA-tag for RBBP6 (yellow). Hoechst staining for nucleus (cyan). Scale
881 bars: 20 μm (main panels), 10 μm (zoom).

882 (E) Western blot for co-IP of NS5 with endogenous RBBP6 or IgG in YFV-infected cells
883 with/without RNaseA treatment. GAPDH is a loading control.

884 (F) Schematic of RBBP6 domain architecture and truncation constructs.

885 (G) Western blot for whole cell lysate and Strep-AP of YFV 2xStrep-tagged NS5 co-transfected
886 with HA-tagged RBBP6 constructs. EV represents an empty vector for negative control.

887 (H) Western blot for whole cell lysate and Strep-AP of YFV 2xStrep-tagged NS5 domain
888 truncations. NS3 and EV are negative controls.

889 (I) *Renilla* luciferase activity of YFV replicon in RBBP6 and control CRISPRi knockdown Huh7
890 cells. Data represent mean ± SD of three biological replicates, with $p < 0.005$ (***), $p < 0.01$ (**),
891 and $p < 0.05$ (*) by one-sided t-test.

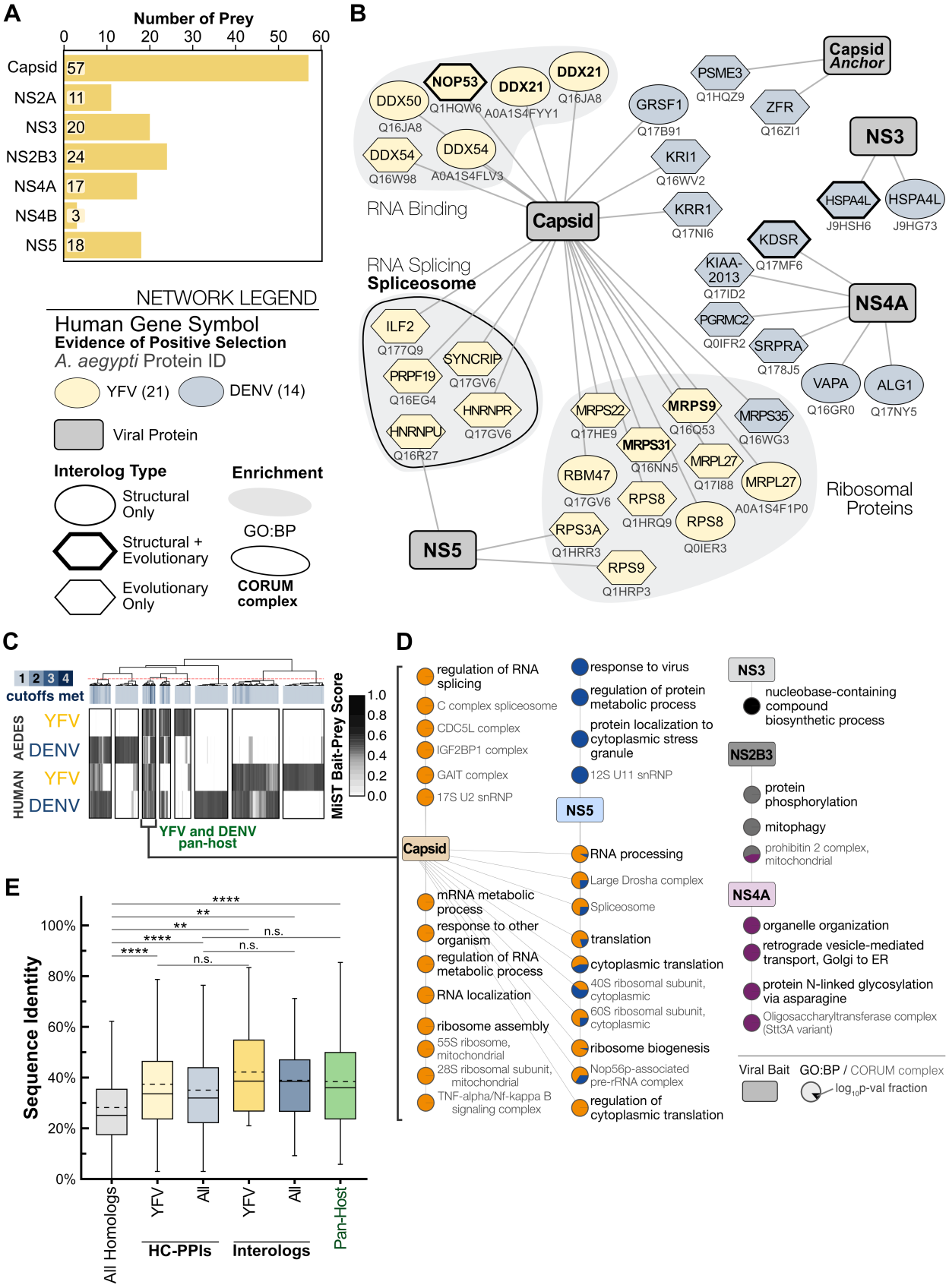
A
Number of Prey
0 10 20 30 40 50 60
Capsid 57
NS2A 11
NS3 20
NS2B3 24
NS4A 17
NS4B 3
NS5 18
NETWORK LEGEND
Human Gene Symbol
Evidence of Positive Selection
A. aegypti Protein ID
YFV (21)
DENV (14)
Viral Protein
Interolog Type
Structural Only
Structural + Evolutionary
Evolutionary Only
Enrichment
GO:BP
CORUM complex
B
Capsid Anchor
NS3
NS4A
NS5
Capsid
RNA Binding
RNA Splicing
Spliceosome
Ribosomal Proteins
NOP53 Q1HQW6
DDX21 A0A1S4FYY1
DDX21 Q16JA8
DDX50 Q16JA8
DDX54 Q16W98
DDX54 A0A1S4FLV3
GRSF1 Q17B91
PSME3 Q1HQZ9
ZFR Q16ZI1
KRI1 Q16WV2
KRR1 Q17NI6
HSPA4L J9HSH6
HSPA4L J9HG73
KDSR Q17MF6
KIAA-2013 Q17ID2
PGRMC2 Q0IFR2
SRPRA Q178J5
VAPA Q16GR0
ALG1 Q17NY5
ILF2 Q177Q9
SYNCRIP Q17GV6
PRPF19 Q16EG4
HNRNPR Q17GV6
HNRNPU Q16R27
MRPS22 Q17HE9
MRPS9 Q16Q53
MRPS35 Q16WG3
MRPS31 Q16NN5
MRPL27 Q17I88
MRPL27 A0A1S4F1P0
RBM47 Q17GV6
RPS8 Q1HRQ9
RPS8 Q0IER3
RPS3A Q1HRR3
RPS9 Q1HRP3
C
1 2 3 4
cutoffs met
AEDES
YFV
DENV
HUMAN
YFV
DENV
MiST Bait-Prey Score
1.0
0.8
0.6
0.4
0.2
0.0
YFV and DENV pan-host
D
regulation of RNA splicing
C complex spliceosome
CDC5L complex
IGF2BP1 complex
GAIT complex
17S U2 snRNP
Capsid
mRNA metabolic process
response to other organism
regulation of RNA metabolic process
RNA localization
ribosome assembly
55S ribosome, mitochondrial
28S ribosomal subunit, mitochondrial
TNF-alpha/Nf-kappa B signaling complex
response to virus
regulation of protein metabolic process
protein localization to cytoplasmic stress granule
12S U11 snRNP
NS5
RNA processing
Large Drosha complex
Spliceosome
translation
cytoplasmic translation
40S ribosomal subunit, cytoplasmic
60S ribosomal subunit, cytoplasmic
ribosome biogenesis
Nop56p-associated pre-rRNA complex
regulation of cytoplasmic translation
NS3
nucleobase-containing compound biosynthetic process
NS2B3
protein phosphorylation
mitophagy
prohibitin 2 complex, mitochondrial
NS4A
organelle organization
retrograde vesicle-mediated transport, Golgi to ER
protein N-linked glycosylation via asparagine
Oligosaccharyltransferase complex (Stt3A variant)
Viral Bait
GO:BP / CORUM complex
log10p-val fraction
E
Sequence Identity
100%
80%
60%
40%
20%
0%
****
**
**
****
****
n.s.
n.s.
n.s.
All Homologs
YFV
All
YFV
All
Pan-Host
HC-PPIs
Interologs

892

893 **Figure 4. Predicted structures and holistic analysis facilitate interolog identification.**

894 (A) Number of HC-PPIs identified per viral bait from mosquito proteomics.

895 (B) Network of structure- and evolutionary-based interologs for both YFV and DENV. The node
896 label is the human gene symbol. The mosquito UniProt ID is listed under the node. Enriched
897 GO:BP categories and CORUM complexes are based on human annotations. Bolded gene IDs
898 indicate proteins found to have positive selection.

899 (C) Hierarchical clustering of flavivirus-mosquito and flavivirus-human PPIs based on MiST
900 scores. Interactions were only considered for viral baits consistently studied across all datasets.
901 An interaction only included if it was a HC-PPI in at least one study and was evaluated for number
902 of studies in which it was considered HC-PPI (cutoffs met shown in blue scale bar). K-means
903 clustering optimized the number of clusters to select a hierarchal cutoff to define clusters (red
904 dashed line).

905 (D) Enrichment network for GO:BP and CORUM complexes from YFV and DENV pan-host
906 cluster, representing interactions conserved across all interactomes analyzed. The color indicates
907 the viral bait associated with the enrichment term and pie sector represents the fractional
908 magnitude of the $\log_{10}$p-value of that enrichment. A monochromatic point indicates it was only
909 significant ($p < 0.05$) for a single viral bait.

910 (E) Box and whisker plots showing the sequence identity values of human-*A. aegypti* homolog
911 pairs of indicated groups of proteins. Solid horizontal lines indicate the median. Dashed horizontal
912 lines indicate the mean. Adjusted p-values were calculated using a Wilcoxon rank-sum test with
913 Bonferroni correction: adjusted $p < 0.0001$ (****), adjusted $p < 0.001$ (***), adjusted $p < 0.01$ (**),
914 adjusted $p < 0.05$ (*), adjusted $p > 0.05$ (n.s.).

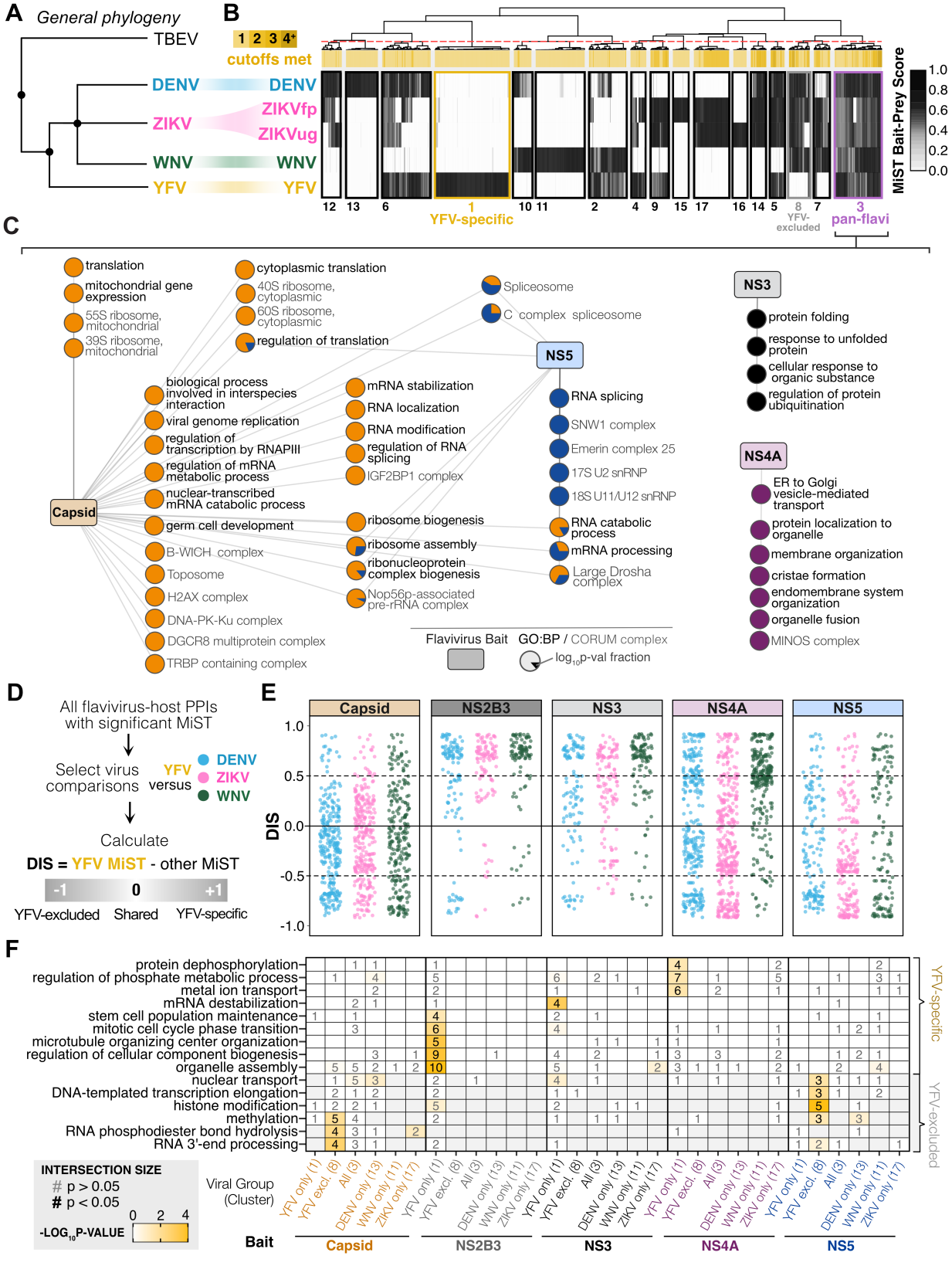
A
General phylogeny
TBEV
DENV
ZIKV
WNV
YFV
B
1 2 3 4+
cutoffs met
DENV
ZIKVfp
ZIKVug
WNV
YFV
MiST Bait-Prey Score
1.0
0.8
0.6
0.4
0.2
0.0
12 13 6 1 10 11 2 4 9 15 17 16 14 5 8 7 3
YFV-specific
YFV-excluded
pan-flavi
C
translation
mitochondrial gene expression
55S ribosome, mitochondrial
39S ribosome, mitochondrial
cytoplasmic translation
40S ribosome, cytoplasmic
60S ribosome, cytoplasmic
regulation of translation
Spliceosome
C complex spliceosome
NS5
NS3
protein folding
response to unfolded protein
cellular response to organic substance
regulation of protein ubiquitination
biological process involved in interspecies interaction
viral genome replication
regulation of transcription by RNAPIII
regulation of mRNA metabolic process
nuclear-transcribed mRNA catabolic process
germ cell development
B-WICH complex
Toposome
H2AX complex
DNA-PK-Ku complex
DGCR8 multiprotein complex
TRBP containing complex
Capsid
mRNA stabilization
RNA localization
RNA modification
regulation of RNA splicing
IGF2BP1 complex
ribosome biogenesis
ribosome assembly
ribonucleoprotein complex biogenesis
Nop56p-associated pre-rRNA complex
RNA splicing
SNW1 complex
Emerin complex 25
17S U2 snRNP
18S U11/U12 snRNP
RNA catabolic process
mRNA processing
Large Drosha complex
NS4A
ER to Golgi vesicle-mediated transport
protein localization to organelle
membrane organization
cristae formation
endomembrane system organization
organelle fusion
MINOS complex
Flavivirus Bait
GO:BP / CORUM complex
log10p-val fraction
D
All flavivirus-host PPIs with significant MiST
Select virus comparisons
YFV versus
DENV
ZIKV
WNV
Calculate
DIS = YFV MiST - other MiST
-1
0
+1
YFV-excluded
Shared
YFV-specific
E
Capsid
NS2B3
NS3
NS4A
NS5
DIS
1.0
0.5
0.0
-0.5
-1.0
F
protein dephosphorylation
regulation of phosphate metabolic process
metal ion transport
mRNA destabilization
stem cell population maintenance
mitotic cell cycle phase transition
microtubule organizing center organization
regulation of cellular component biogenesis
organelle assembly
nuclear transport
DNA-templated transcription elongation
histone modification
methylation
RNA phosphodiester bond hydrolysis
RNA 3'-end processing
YFV-specific
YFV-excluded
INTERSECTION SIZE
p > 0.05
# p < 0.05
-LOG10P-VALUE
0 2 4
Viral Group (Cluster)
YFV only (1)
YFV excl. (8)
All (3)
DENV only (13)
WNV only (11)
ZIKV only (17)
Bait
Capsid
NS2B3
NS3
NS4A
NS5

916 **Figure 5. Holistic integration of flavivirus-host interactomes reveals pan-flavivirus and**
917 **divergent mechanisms of host targeting.**

918 (A) Approximate evolutionary relationship between DENV, ZIKV, WNV, and YFV. TBEV was
919 included to represent a true outgroup compared to mosquito-borne flaviviruses.

920 (B) Hierarchical clustering of flavivirus-human PPIs based on MiST scores. Interactions were
921 only considered for viral baits consistently studied across all viruses. An interaction was only
922 included if it was a HC-PPI in at least one study and was evaluated for the number of studies in
923 which it was considered HC-PPI (cutoffs met shown in yellow scale bar). K-means clustering
924 optimized the number of clusters to select a hierarchal cutoff to define clusters (red dashed
925 line).

926 (C) Enrichment network for GO:BP and CORUM complexes from cluster 3, representing pan-
927 flavivirus interactions conserved across all interactomes analyzed. The color indicates the viral
928 bait associated with the enrichment term, and the pie sector represents the fractional magnitude
929 of the $\log_{10}$p-value of that enrichment. A monochromatic point indicates it was only significant (p
930 < 0.05) for a single viral bait.

931 (D) Schematic of differential interaction score (DIS) calculation.

932 (E) Plot of YFV DIS distributions, separated by the viral bait. Dot colors indicate the virus used for
933 DIS comparison.

934 (F) Heatmap showing the degree of enrichment ($\log_{10}$p-value, yellow scale bar) for unique terms
935 in clusters associated with YFV specifically (cluster 1) or excluding YFV (cluster 8), grouped by
936 viral bait. Enrichment terms were excluded if they showed significant enrichment for other
937 clusters. Other clusters are included in the heatmap to demonstrate the enrichment is unique to
938 clusters 1 or 8. In each tile, the number of interactions associated with that enrichment term is
939 bolded if it was significant ($p < 0.05$).

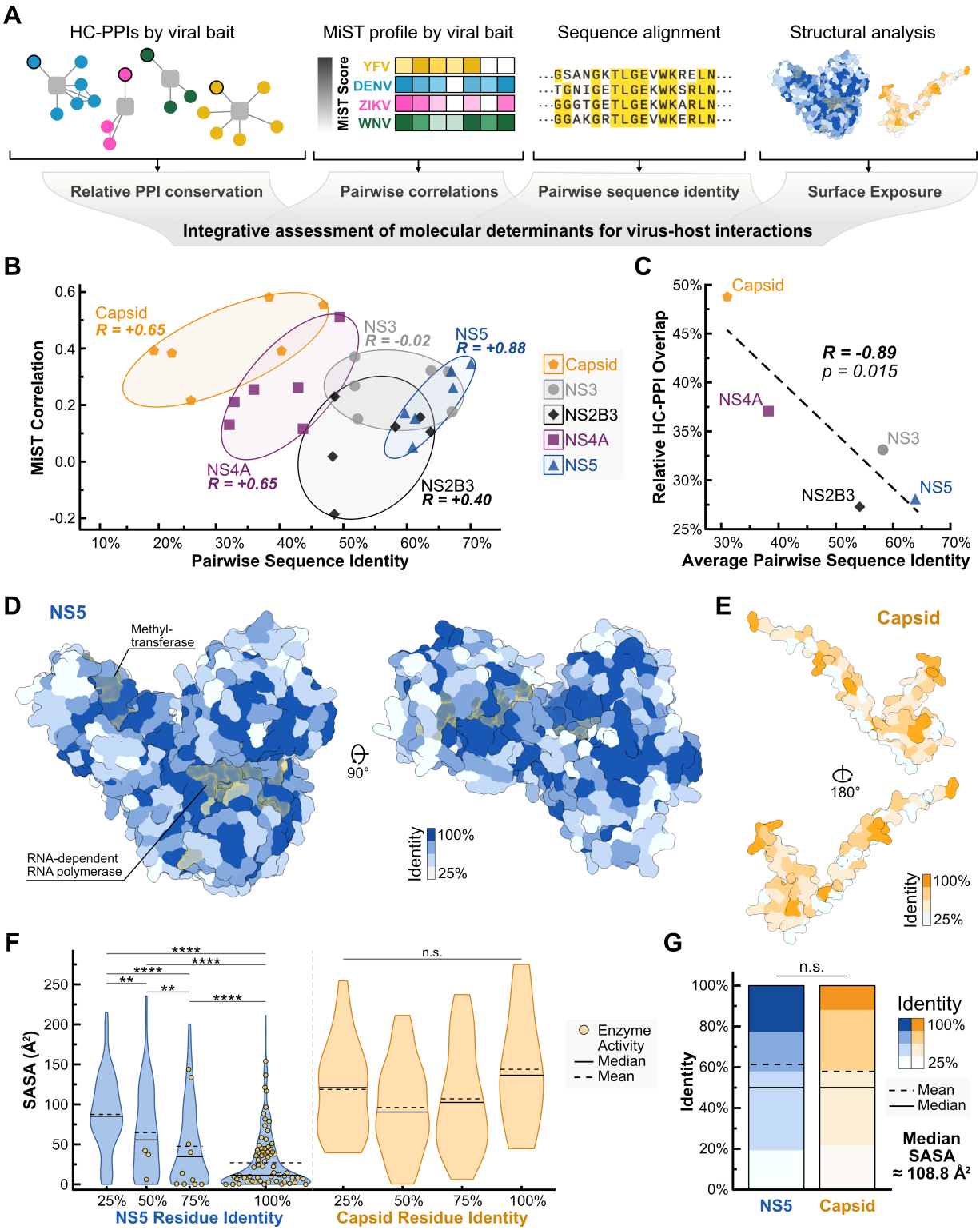

Figure 6. Integration of virus sequence and structure reveals a complex relationship with PPI conservation

943 (A) Schematic of PPI, sequence, and structural analysis. PPIs were analyzed according to viral
944 baits across all four flavivirus-host PPI datasets.
945 (B) Pearson's correlation between MiST score profiles and viral protein sequence conservation.
946 For each viral bait, six pairwise correlations were calculated for MiST profiles for each possible
947 pairwise combination between four viruses. The same was done for pairwise sequence identity.
948 Pearson's correlations between MiST correlations and sequence identity were then calculated for
949 each viral bait and the entire dataset.
950 (C) Pearson's correlation between relative HC-PPI conservation and viral protein sequence
951 conservation. For each viral bait, mean values of relative HC-PPI conservation and pairwise
952 sequence identity were plotted.
953 (D-E) Visualization of YFV NS5 and Capsid protein structures with protein sequence
954 conservation. Residues with known enzymatic activity are colored with a yellow overlay.
955 Structures were generated using the YFV-Asibi protein sequence and AlphaFold2.
956 (F) Violin plot of solvent accessible surface area (SASA) binned by amino acid conservation for
957 NS5 and Capsid. Yellow dots indicate residues with known enzyme activity. Solid horizontal lines
958 indicate the median. Dashed horizontal lines indicate the mean. Adjusted p-values were
959 calculated using a Wilcoxon rank-sum test with Bonferroni correction: adjusted $p < 0.0001$ (****),
960 adjusted $p < 0.001$ (***), adjusted $p < 0.01$ (**), adjusted $p < 0.05$ (*), adjusted $p > 0.05$ (n.s).
961 (G) Stacked bar plot of the distribution of amino acid identity. Only NS5 amino acids with similar
962 SASA as Capsid were considered. P-value was calculated using a Wilcoxon rank-sum (Mann-
963 Whitney U) test: $p > 0.05$ (n.s).

964 # References

965 1. Pierson, T.C., and Diamond, M.S. (2020). The continued threat of emerging flaviviruses. Nat
966 Microbiol *5*, 796–812. https://doi.org/10.1038/s41564-020-0714-0.

967 2. Ryan, S.J., Carlson, C.J., Mordecai, E.A., and Johnson, L.R. (2019). Global expansion and
968 redistribution of Aedes-borne virus transmission risk with climate change. PLOS Neglected
969 Tropical Diseases *13*, e0007213. https://doi.org/10.1371/journal.pntd.0007213.

970 3. Mordecai, E.A., Ryan, S.J., Caldwell, J.M., Shah, M.M., and LaBeaud, A.D. (2020). Climate
971 change could shift disease burden from malaria to arboviruses in Africa. The Lancet
972 Planetary Health *4*, e416–e423. https://doi.org/10.1016/S2542-5196(20)30178-9.

973 4. Kolimenakis, A., Heinz, S., Wilson, M.L., Winkler, V., Yakob, L., Michaelakis, A., Papachristos,
974 D., Richardson, C., and Horstick, O. (2021). The role of urbanisation in the spread of Aedes
975 mosquitoes and the diseases they transmit—A systematic review. PLOS Neglected Tropical
976 Diseases *15*, e0009631. https://doi.org/10.1371/journal.pntd.0009631.

977 5. Pandit, P.S., Doyle, M.M., Smart, K.M., Young, C.C.W., Drape, G.W., and Johnson, C.K.
978 (2018). Predicting wildlife reservoirs and global vulnerability to zoonotic Flaviviruses. Nat
979 Commun *9*, 5425. https://doi.org/10.1038/s41467-018-07896-2.

980 6. Komarasamy, T.V., Adnan, N.A.A., James, W., and Balasubramaniam, V.R. (2022). Finding a
981 chink in the armor: Update, limitations, and challenges toward successful antivirals against
982 flaviviruses. PLOS Neglected Tropical Diseases *16*, e0010291.
983 https://doi.org/10.1371/journal.pntd.0010291.

984 7. Cakir, M., Obernier, K., Forget, A., and Krogan, N.J. Target Discovery for Host-Directed
985 Antiviral Therapies: Application of Proteomics Approaches. mSystems *6*, e00388-21.
986 https://doi.org/10.1128/mSystems.00388-21.

987 8. Fishburn, A.T., Pham, O.H., Kenaston, M.W., Beesabathuni, N.S., and Shah, P.S. (2022). Let's
988 Get Physical: Flavivirus-Host Protein–Protein Interactions in Replication and Pathogenesis.
989 Frontiers in Microbiology *13*.

990 9. Shah, P.S., Beesabathuni, N.S., Fishburn, A.T., Kenaston, M.W., Minami, S.A., Pham, O.H.,
991 and Tucker, I. (2022). Systems Biology of Virus-Host Protein Interactions: From Hypothesis
992 Generation to Mechanisms of Replication and Pathogenesis. Annual Review of Virology *9*,
993 397–415. https://doi.org/10.1146/annurev-virology-100520-011851.

994 10. Petit, M.J., and Shah, P.S. (2019). Mapping Arbovirus-Vector Interactions Using Systems
995 Biology Techniques. Front. Cell. Infect. Microbiol. *8*.
996 https://doi.org/10.3389/fcimb.2018.00440.

11. Li, M., Ramage, H., and Cherry, S. (2020). Deciphering flavivirus-host interactions using quantitative proteomics. Curr Opin Immunol *66*, 90–97. https://doi.org/10.1016/j.coi.2020.06.002.

12. Gotuzzo, E., Yactayo, S., and Córdova, E. (2013). Efficacy and Duration of Immunity after Yellow Fever Vaccination: Systematic Review on the Need for a Booster Every 10 Years. Am J Trop Med Hyg *89*, 434–444. https://doi.org/10.4269/ajtmh.13-0264.

13. Rosenstein, M.D., de Visser, A.W., Visser, L.G., and Roukens, A.H.E. (2021). Long-term immunity after a single yellow fever vaccination in travelers vaccinated at 60 years or older: A 10-year follow-up study. Journal of Travel Medicine *28*, taab126. https://doi.org/10.1093/jtm/taab126.

14. Couto-Lima, D., Madec, Y., Bersot, M.I., Campos, S.S., Motta, M. de A., Santos, F.B. dos, Vazeille, M., Vasconcelos, P.F. da C., Lourenço-de-Oliveira, R., and Failloux, A.-B. (2017). Potential risk of re-emergence of urban transmission of Yellow Fever virus in Brazil facilitated by competent Aedes populations. Sci Rep *7*, 4848. https://doi.org/10.1038/s41598-017-05186-3.

15. Faria, N.R., Kraemer, M.U.G., Hill, S.C., Goes de Jesus, J., Aguiar, R.S., Iani, F.C.M., Xavier, J., Quick, J., du Plessis, L., Dellicour, S., et al. (2018). Genomic and epidemiological monitoring of yellow fever virus transmission potential. Science *361*, 894–899. https://doi.org/10.1126/science.aat7115.

16. Gaythorpe, K.A., Hamlet, A., Cibrelus, L., Garske, T., and Ferguson, N.M. (2020). The effect of climate change on yellow fever disease burden in Africa. eLife *9*, e55619. https://doi.org/10.7554/eLife.55619.

17. Gaythorpe, K.A., Hamlet, A., Jean, K., Garkauskas Ramos, D., Cibrelus, L., Garske, T., and Ferguson, N. (2021). The global burden of yellow fever. eLife *10*, e64670. https://doi.org/10.7554/eLife.64670.

18. Epidemiological Alert Yellow fever in the Americas Region - 3 February 2025 - PAHO/WHO | Pan American Health Organization (2025). https://www.paho.org/en/documents/epidemiological-alert-yellow-fever-americas-region-3-february-2025.

19. Cunha, M.S., Guerra, J.M., Siconelli, M.J.L., Fonseca, B.A.L. da, Dias, J.C. de A., Freitas, G.D. de, Sabino, E., Manulli, E.R., Pereira, G.M., Valença, I.N., et al. (2025). Yellow fever virus resurgence in São Paulo State, Brazil, 2024-2025. Preprint at medRxiv, https://doi.org/10.1101/2025.03.14.25323956.

20. Alkan, C., Zapata, S., Bichaud, L., Moureau, G., Lemey, P., Firth, A.E., Gritsun, T.S., Gould, E.A., de Lamballerie, X., Depaquit, J., et al. (2015). Ecuador Paraiso Escondido Virus, a New Flavivirus Isolated from New World Sand Flies in Ecuador, Is the First Representative of a

1033 Novel Clade in the Genus Flavivirus. J Virol *89*, 11773–11785.
1034 https://doi.org/10.1128/JVI.01543-15.

1035 21. Gould, E.A., de Lamballerie, X., Zanotto, P.M. de A., and Holmes, E.C. (2003). Origins,
1036 evolution, and vector/host coadaptations within the Genus Flavivirus. In Advances in
1037 Virus Research (Academic Press), pp. 277–314. https://doi.org/10.1016/S0065-
1038 3527(03)59008-X.

1039 22. Shah, P.S., Link, N., Jang, G.M., Sharp, P.P., Zhu, T., Swaney, D.L., Johnson, J.R., Von Dollen,
1040 J., Ramage, H.R., Satkamp, L., et al. (2018). Comparative Flavivirus-Host Protein Interaction
1041 Mapping Reveals Mechanisms of Dengue and Zika Virus Pathogenesis. Cell *175*, 1931-
1042 1945.e18. https://doi.org/10.1016/j.cell.2018.11.028.

1043 23. Li, M., Johnson, J.R., Truong, B., Kim, G., Weinbren, N., Dittmar, M., Shah, P.S., Von Dollen,
1044 J., Newton, B.W., Jang, G.M., et al. (2019). Identification of Antiviral Roles for the Exon-
1045 Junction Complex and Nonsense-Mediated Decay in Flaviviral Infection. Nat Microbiol *4*,
1046 985–995. https://doi.org/10.1038/s41564-019-0375-z.

1047 24. Scaturro, P., Stukalov, A., Haas, D.A., Cortese, M., Draganova, K., Płaszczyca, A.,
1048 Bartenschlager, R., Götz, M., and Pichlmair, A. (2018). An orthogonal proteomic survey
1049 uncovers novel Zika virus host factors. Nature *561*, 253–257.
1050 https://doi.org/10.1038/s41586-018-0484-5.

1051 25. Lichinchi, G., Zhao, B.S., Wu, Y., Lu, Z., Qin, Y., He, C., and Rana, T.M. (2016). Dynamics of
1052 Human and Viral RNA Methylation during Zika Virus Infection. Cell Host Microbe *20*, 666–
1053 673. https://doi.org/10.1016/j.chom.2016.10.002.

1054 26. Gokhale, N.S., McIntyre, A.B.R., McFadden, M.J., Roder, A.E., Kennedy, E.M., Gandara, J.A.,
1055 Hopcraft, S.E., Quicke, K.M., Vazquez, C., Willer, J., et al. (2016). N6-Methyladenosine in
1056 Flaviviridae Viral RNA Genomes Regulates Infection. Cell Host Microbe *20*, 654–665.
1057 https://doi.org/10.1016/j.chom.2016.09.015.

1058 27. Ooi, Y.S., Majzoub, K., Flynn, R.A., Mata, M.A., Diep, J., Li, J.K., van Buuren, N., Rumachik, N.,
1059 Johnson, A.G., Puschnik, A.S., et al. (2019). An RNA-centric dissection of host complexes
1060 controlling flavivirus infection. Nat Microbiol *4*, 2369–2382.
1061 https://doi.org/10.1038/s41564-019-0518-2.

1062 28. Li, P., Wu, J., Liu, S., Lu, R., Jiang, H., Wang, N., Luo, M., Guo, L., Xiao, J., Bu, L., et al. (2022).
1063 The RNA polymerase of cytoplasmically replicating Zika virus binds with chromatin DNA in
1064 nuclei and regulates host gene transcription. Proc Natl Acad Sci U S A *119*, e2205013119.
1065 https://doi.org/10.1073/pnas.2205013119.

1066 29. Yu, C.-Y., Hsu, Y.-W., Liao, C.-L., and Lin, Y.-L. (2006). Flavivirus infection activates the XBP1
1067 pathway of the unfolded protein response to cope with endoplasmic reticulum stress. J
1068 Virol *80*, 11868–11880. https://doi.org/10.1128/JVI.00879-06.

1069 30. Li, M.Y., Naik, T.S., Siu, L.Y.L., Acuto, O., Spooner, E., Wang, P., Yang, X., Lin, Y., Bruzzone, R.,
1070 Ashour, J., et al. (2020). Lyn kinase regulates egress of flaviviruses in autophagosome-
1071 derived organelles. Nat Commun *11*, 5189. https://doi.org/10.1038/s41467-020-19028-w.

1072 31. Yau, W.-L., Peters, M.B.A., Sorin, M., Rönfeldt, S., Pulkkinen, L.I.A., Carlson, L.-A., Överby,
1073 A.K., and Lundmark, R. (2024). The flavivirus protein NS4B recruits the cis-Golgi protein
1074 ACBD3 to modify ER-Golgi trafficking for virion release. Preprint at bioRxiv,
1075 https://doi.org/10.1101/2024.04.03.587877 https://doi.org/10.1101/2024.04.03.587877.

1076 32. Petit, M.J., Kenaston, M.W., Pham, O.H., Nagainis, A.A., Fishburn, A.T., and Shah, P.S.
1077 (2021). Nuclear dengue virus NS5 antagonizes expression of PAF1-dependent immune
1078 response genes. PLOS Pathogens *17*, e1010100.
1079 https://doi.org/10.1371/journal.ppat.1010100.

1080 33. De Maio, F.A., Risso, G., Iglesias, N.G., Shah, P., Pozzi, B., Gebhard, L.G., Mammi, P.,
1081 Mancini, E., Yanovsky, M.J., Andino, R., et al. (2016). The Dengue Virus NS5 Protein
1082 Intrudes in the Cellular Spliceosome and Modulates Splicing. PLoS Pathog *12*, e1005841.
1083 https://doi.org/10.1371/journal.ppat.1005841.

1084 34. Fontaine, K.A., Leon, K.E., Khalid, M.M., Tomar, S., Jimenez-Morales, D., Dunlap, M., Kaye,
1085 J.A., Shah, P.S., Finkbeiner, S., Krogan, N.J., et al. (2018). The Cellular NMD Pathway
1086 Restricts Zika Virus Infection and Is Targeted by the Viral Capsid Protein. mBio *9*, e02126-
1087 18. https://doi.org/10.1128/mBio.02126-18.

1088 35. Ohlson, M.B., Eitson, J.L., Wells, A.I., Kumar, A., Jang, S., Ni, C., Xing, C., Buszczak, M., and
1089 Schoggins, J.W. Genome-Scale CRISPR Screening Reveals Host Factors Required for
1090 Ribosome Formation and Viral Replication. mBio *14*, e00127-23.
1091 https://doi.org/10.1128/mbio.00127-23.

1092 36. Ngo, A.M., Shurtleff, M.J., Popova, K.D., Kulsuptrakul, J., Weissman, J.S., and Puschnik, A.S.
1093 (2019). The ER membrane protein complex is required to ensure correct topology and
1094 stable expression of flavivirus polyproteins. Elife *8*, e48469.
1095 https://doi.org/10.7554/eLife.48469.

1096 37. Zhang, R., Miner, J.J., Gorman, M.J., Rausch, K., Ramage, H., White, J.P., Zuiani, A., Zhang, P.,
1097 Fernandez, E., Zhang, Q., et al. (2016). A CRISPR screen defines a signal peptide processing
1098 pathway required by flaviviruses. Nature *535*, 164–168.
1099 https://doi.org/10.1038/nature18625.

1100 38. Tsitsiridis, G., Steinkamp, R., Giurgiu, M., Brauner, B., Fobo, G., Frishman, G., Montrone, C.,
1101 and Ruepp, A. (2023). CORUM: the comprehensive resource of mammalian protein
1102 complexes–2022. Nucleic Acids Research *51*, D539–D545.
1103 https://doi.org/10.1093/nar/gkac1015.

1104 39. Marceau, C.D., Puschnik, A.S., Majzoub, K., Ooi, Y.S., Brewer, S.M., Fuchs, G., Swaminathan,
1105 K., Mata, M.A., Elias, J.E., Sarnow, P., et al. (2016). Genetic dissection of Flaviviridae host
1106 factors through genome-scale CRISPR screens. Nature *535*, 159–163.
1107 https://doi.org/10.1038/nature18631.

1108 40. Sessions, O.M., Barrows, N.J., Souza-Neto, J.A., Robinson, T.J., Hershey, C.L., Rodgers, M.A.,
1109 Ramirez, J.L., Dimopoulos, G., Yang, P.L., Pearson, J.L., et al. (2009). Discovery of insect and
1110 human dengue virus host factors. Nature *458*, 1047–1050.
1111 https://doi.org/10.1038/nature07967.

1112 41. Krishnan, M.N., Ng, A., Sukumaran, B., Gilfoy, F.D., Uchil, P.D., Sultana, H., Brass, A.L.,
1113 Adametz, R., Tsui, M., Qian, F., et al. (2008). RNA interference screen for human genes
1114 associated with West Nile virus infection. Nature *455*, 242–245.
1115 https://doi.org/10.1038/nature07207.

1116 42. Savidis, G., McDougall, W.M., Meraner, P., Perreira, J.M., Portmann, J.M., Trincucci, G.,
1117 John, S.P., Aker, A.M., Renzette, N., Robbins, D.R., et al. (2016). Identification of Zika Virus
1118 and Dengue Virus Dependency Factors using Functional Genomics. Cell Reports *16*, 232–
1119 246. https://doi.org/10.1016/j.celrep.2016.06.028.

1120 43. Hahn, C.S., Dalrymple, J.M., Strauss, J.H., and Rice, C.M. (1987). Comparison of the virulent
1121 Asibi strain of yellow fever virus with the 17D vaccine strain derived from it. Proc Natl
1122 Acad Sci U S A *84*, 2019–2023. https://doi.org/10.1073/pnas.84.7.2019.

1123 44. De Brito, T., Siqueira, S.A., Santos, R.T., Nassar, E.S., Coimbra, T.L., and Alves, V.A. (1992).
1124 Human fatal yellow fever. Immunohistochemical detection of viral antigens in the liver,
1125 kidney and heart. Pathol Res Pract *188*, 177–181. https://doi.org/10.1016/S0344-
1126 0338(11)81176-3.

1127 45. Lefeuvre, A., Contamin, H., Decelle, T., Fournier, C., Lang, J., Deubel, V., and Marianneau, P.
1128 (2006). Host-cell interaction of attenuated and wild-type strains of yellow fever virus can
1129 be differentiated at early stages of hepatocyte infection. Microbes and Infection *8*, 1530–
1130 1538. https://doi.org/10.1016/j.micinf.2006.01.013.

1131 46. Woodson, S.E., and Holbrook, M.R. (2011). Infection of hepatocytes with 17-D vaccine-
1132 strain yellow fever virus induces a strong pro-inflammatory host response. J Gen Virol *92*,
1133 2262–2271. https://doi.org/10.1099/vir.0.031617-0.

1134 47. Pugh, D.J.R., Ab, E., Faro, A., Lutya, P.T., Hoffmann, E., and Rees, D.J.G. (2006). DWNN, a
1135 novel ubiquitin-like domain, implicates RBBP6 in mRNA processing and ubiquitin-like
1136 pathways. BMC Struct Biol *6*, 1. https://doi.org/10.1186/1472-6807-6-1.

1137 48. Chibi, M., Meyer, M., Skepu, A., G. Rees, D.J., Moolman-Smook, J.C., and Pugh, D.J.R.
1138 (2008). RBBP6 Interacts with Multifunctional Protein YB-1 through Its RING Finger Domain,

1139 Leading to Ubiquitination and Proteosomal Degradation of YB-1. Journal of Molecular
1140 Biology *384*, 908–916. https://doi.org/10.1016/j.jmb.2008.09.060.

1141 49. Li, L., Deng, B., Xing, G., Teng, Y., Tian, C., Cheng, X., Yin, X., Yang, J., Gao, X., Zhu, Y., et al.
1142 (2007). PACT is a negative regulator of p53 and essential for cell growth and embryonic
1143 development. Proceedings of the National Academy of Sciences *104*, 7951–7956.
1144 https://doi.org/10.1073/pnas.0701916104.

1145 50. Jones, C.T., Patkar, C.G., and Kuhn, R.J. (2005). Construction and applications of yellow fever
1146 virus replicons. Virology *331*, 247–259. https://doi.org/10.1016/j.virol.2004.10.034.

1147 51. Sawyer, S.L., Wu, L.I., Emerman, M., and Malik, H.S. (2005). Positive selection of primate
1148 TRIM5alpha identifies a critical species-specific retroviral restriction domain. Proc Natl
1149 Acad Sci U S A *102*, 2832–2837. https://doi.org/10.1073/pnas.0409853102.

1150 52. Kerns, J.A., Emerman, M., and Malik, H.S. (2008). Positive selection and increased antiviral
1151 activity associated with the PARP-containing isoform of human zinc-finger antiviral
1152 protein. PLoS Genet *4*, e21. https://doi.org/10.1371/journal.pgen.0040021.

1153 53. Duggal, N.K., and Emerman, M. (2012). Evolutionary conflicts between viruses and
1154 restriction factors shape immunity. Nat Rev Immunol *12*, 687–695.
1155 https://doi.org/10.1038/nri3295.

1156 54. Daugherty, M.D., and Malik, H.S. (2012). Rules of engagement: molecular insights from
1157 host-virus arms races. Annu Rev Genet *46*, 677–700. https://doi.org/10.1146/annurev-
1158 genet-110711-155522.

1159 55. Fredericks, A.C., Russell, T.A., Wallace, L.E., Davidson, A.D., Fernandez-Sesma, A., and
1160 Maringer, K. (2019). Aedes aegypti (Aag2)-derived clonal mosquito cell lines reveal the
1161 effects of pre-existing persistent infection with the insect-specific bunyavirus Phasi
1162 Charoen-like virus on arbovirus replication. PLoS Negl Trop Dis *13*, e0007346.
1163 https://doi.org/10.1371/journal.pntd.0007346.

1164 56. Brito, A.F., and Pinney, J.W. (2017). Protein–Protein Interactions in Virus–Host Systems.
1165 Frontiers in Microbiology *8*.

1166 57. Kim, W., Mirdita, M., Levy Karin, E., Gilchrist, C.L.M., Schweke, H., Söding, J., Levy, E.D., and
1167 Steinegger, M. (2025). Rapid and sensitive protein complex alignment with Foldseek-
1168 Multimer. Nat Methods. https://doi.org/10.1038/s41592-025-02593-7.

1169 58. van Kempen, M., Kim, S.S., Tumescheit, C., Mirdita, M., Lee, J., Gilchrist, C.L.M., Söding, J.,
1170 and Steinegger, M. (2024). Fast and accurate protein structure search with Foldseek. Nat
1171 Biotechnol *42*, 243–246. https://doi.org/10.1038/s41587-023-01773-0.

1172 59. Li, Z., Jaroszewski, L., Iyer, M., Sedova, M., and Godzik, A. (2020). FATCAT 2.0: towards a
1173 better understanding of the structural diversity of proteins. Nucleic Acids Res *48*, W60–
1174 W64. https://doi.org/10.1093/nar/gkaa443.

1175 60. Sonnhammer, E.L.L., and Östlund, G. (2015). InParanoid 8: orthology analysis between 273
1176 proteomes, mostly eukaryotic. Nucleic Acids Res *43*, D234–D239.
1177 https://doi.org/10.1093/nar/gku1203.

1178 61. Garamszegi, S., Franzosa, E.A., and Xia, Y. (2013). Signatures of Pleiotropy, Economy and
1179 Convergent Evolution in a Domain-Resolved Map of Human–Virus Protein–Protein
1180 Interaction Networks. PLOS Pathogens *9*, e1003778.
1181 https://doi.org/10.1371/journal.ppat.1003778.

1182 62. Bouhaddou, M., Reuschl, A.-K., Polacco, B.J., Thorne, L.G., Ummadi, M.R., Ye, C., Rosales, R.,
1183 Pelin, A., Batra, J., Jang, G.M., et al. (2023). SARS-CoV-2 variants evolve convergent
1184 strategies to remodel the host response. Cell *186*, 4597-4614.e26.
1185 https://doi.org/10.1016/j.cell.2023.08.026.

1186 63. Elhabashy, H., Merino, F., Alva, V., Kohlbacher, O., and Lupas, A.N. (2022). Exploring
1187 protein-protein interactions at the proteome level. Structure *30*, 462–475.
1188 https://doi.org/10.1016/j.str.2022.02.004.

1189 64. Gordon, D.E., Hiatt, J., Bouhaddou, M., Rezelj, V.V., Ulferts, S., Braberg, H., Jureka, A.S.,
1190 Obernier, K., Guo, J.Z., Batra, J., et al. (2020). Comparative host-coronavirus protein
1191 interaction networks reveal pan-viral disease mechanisms. Science *370*, eabe9403.
1192 https://doi.org/10.1126/science.abe9403.

1193 65. Beauclair, G., Streicher, F., Chazal, M., Bruni, D., Lesage, S., Gracias, S., Bourgeau, S.,
1194 Sinigaglia, L., Fujita, T., Meurs, E.F., et al. (2020). Retinoic Acid Inducible Gene I and Protein
1195 Kinase R, but Not Stress Granules, Mediate the Proinflammatory Response to Yellow Fever
1196 Virus. J Virol *94*, e00403-20. https://doi.org/10.1128/JVI.00403-20.

1197 66. Bonenfant, G., Williams, N., Netzband, R., Schwarz, M.C., Evans, M.J., and Pager, C.T.
1198 (2019). Zika Virus Subverts Stress Granules To Promote and Restrict Viral Gene Expression.
1199 J Virol *93*, e00520-19. https://doi.org/10.1128/JVI.00520-19.

1200 67. Amorim, R., Temzi, A., Griffin, B.D., and Mouland, A.J. (2017). Zika virus inhibits eIF2α-
1201 dependent stress granule assembly. PLOS Neglected Tropical Diseases *11*, e0005775.
1202 https://doi.org/10.1371/journal.pntd.0005775.

1203 68. Gonzalez Lopez Ledesma, M.M., Costa Navarro, G., Pallares, H.M., Paletta, A., De Maio, F.,
1204 Iglesias, N.G., Gebhard, L., Oviedo Rouco, S., Ojeda, D.S., de Borba, L., et al. (2023). Dengue
1205 virus NS5 degrades ERC1 during infection to antagonize NF-kB activation. Proceedings of
1206 the National Academy of Sciences *120*, e2220005120.
1207 https://doi.org/10.1073/pnas.2220005120.

1208 69. Ashour, J., Laurent-Rolle, M., Shi, P.-Y., and García-Sastre, A. (2009). NS5 of dengue virus
1209 mediates STAT2 binding and degradation. J Virol *83*, 5408–5418.
1210 https://doi.org/10.1128/JVI.02188-08.

1211 70. Agarwal, A., Alam, M.F., Basu, B., Pattanayak, S., Asthana, S., Syed, G.H., Kalia, M., and Vrati,
1212 S. (2022). Japanese Encephalitis Virus NS4A Protein Interacts with PTEN-Induced Kinase 1
1213 (PINK1) and Promotes Mitophagy in Infected Cells. Microbiol Spectr *10*, e0083022.
1214 https://doi.org/10.1128/spectrum.00830-22.

1215 71. Ponia, S.S., Robertson, S.J., McNally, K.L., Subramanian, G., Sturdevant, G.L., Lewis, M.,
1216 Jessop, F., Kendall, C., Gallegos, D., Hay, A., et al. (2021). Mitophagy antagonism by ZIKV
1217 reveals Ajuba as a regulator of PINK1 signaling, PKR-dependent inflammation, and viral
1218 invasion of tissues. Cell Rep *37*, 109888. https://doi.org/10.1016/j.celrep.2021.109888.

1219 72. Shuler, G., and Hagai, T. (2022). Rapidly evolving viral motifs mostly target biophysically
1220 constrained binding pockets of host proteins. Cell Reports *40*, 111212.
1221 https://doi.org/10.1016/j.celrep.2022.111212.

1222 73. Miller, S., Kastner, S., Krijnse-Locker, J., Bühler, S., and Bartenschlager, R. (2007). The Non-
1223 structural Protein 4A of Dengue Virus Is an Integral Membrane Protein Inducing
1224 Membrane Alterations in a 2K-regulated Manner*. Journal of Biological Chemistry *282*,
1225 8873–8882. https://doi.org/10.1074/jbc.M609919200.

1226 74. Roosendaal, J., Westaway, E.G., Khromykh, A., and Mackenzie, J.M. (2006). Regulated
1227 Cleavages at the West Nile Virus NS4A-2K-NS4B Junctions Play a Major Role in Rearranging
1228 Cytoplasmic Membranes and Golgi Trafficking of the NS4A Protein. J Virol *80*, 4623–4632.
1229 https://doi.org/10.1128/JVI.80.9.4623-4632.2006.

1230 75. Forst, C.V., Martin-Sancho, L., Tripathi, S., Wang, G., Dos Anjos Borges, L.G., Wang, M.,
1231 Geber, A., Lashua, L., Ding, T., Zhou, X., et al. (2022). Common and species-specific
1232 molecular signatures, networks, and regulators of influenza virus infection in mice, ferrets,
1233 and humans. Science Advances *8*, eabm5859. https://doi.org/10.1126/sciadv.abm5859.

1234 76. Haas, K.M., McGregor, M.J., Bouhaddou, M., Polacco, B.J., Kim, E.-Y., Nguyen, T.T., Newton,
1235 B.W., Urbanowski, M., Kim, H., Williams, M.A.P., et al. (2023). Proteomic and genetic
1236 analyses of influenza A viruses identify pan-viral host targets. Nat Commun *14*, 6030.
1237 https://doi.org/10.1038/s41467-023-41442-z.

1238 77. Batra, J., Hultquist, J.F., Liu, D., Shtanko, O., Von Dollen, J., Satkamp, L., Jang, G.M., Luthra,
1239 P., Schwarz, T.M., Small, G.I., et al. (2018). Protein Interaction Mapping Identifies RBBP6 as
1240 a Negative Regulator of Ebola Virus Replication. Cell *175*, 1917-1930.e13.
1241 https://doi.org/10.1016/j.cell.2018.08.044.

1242 78. Kouno, T., Shibata, S., Shigematsu, M., Hyun, J., Kim, T.G., Matsuo, H., and Wolf, M. (2023).
1243 Structural insights into RNA bridging between HIV-1 Vif and antiviral factor APOBEC3G.
1244 Nat Commun *14*, 4037. https://doi.org/10.1038/s41467-023-39796-5.

1245 79. Ito, F., Alvarez-Cabrera, A.L., Liu, S., Yang, H., Shiriaeva, A., Zhou, Z.H., and Chen, X.S. (2023).
1246 Structural basis for HIV-1 antagonism of host APOBEC3G via Cullin E3 ligase. Sci Adv *9*,
1247 eade3168. https://doi.org/10.1126/sciadv.ade3168.

1248 80. Jones, E., Dillon, B., Swan, D., and Thachil, J. (2022). Practical management of the
1249 haemorrhagic complications of myeloproliferative neoplasms. Br J Haematol *199*, 313–
1250 321. https://doi.org/10.1111/bjh.18322.

1251 81. Harutyunyan, A.S., Giambruno, R., Krendl, C., Stukalov, A., Klampfl, T., Berg, T., Chen, D.,
1252 Milosevic Feenstra, J.D., Jäger, R., Gisslinger, B., et al. (2016). Germline RBBP6 mutations in
1253 familial myeloproliferative neoplasms. Blood *127*, 362–365.
1254 https://doi.org/10.1182/blood-2015-09-668673.

1255 82. Link, N., Chung, H., Jolly, A., Withers, M., Tepe, B., Arenkiel, B.R., Shah, P.S., Krogan, N.J.,
1256 Aydin, H., Geckinli, B.B., et al. (2019). Mutations in ANKLE2, a ZIKA Virus Target, Disrupt an
1257 Asymmetric Cell Division Pathway in Drosophila Neuroblasts to Cause Microcephaly. Dev
1258 Cell *51*, 713-729.e6. https://doi.org/10.1016/j.devcel.2019.10.009.

1259 83. Messaoudi, I., and Basler, C.F. (2015). Immunological features underlying viral hemorrhagic
1260 fevers. Current Opinion in Immunology *36*, 38–46.
1261 https://doi.org/10.1016/j.coi.2015.06.003.

1262 84. Karniely, S., Weekes, M.P., Antrobus, R., Rorbach, J., van Haute, L., Umrania, Y., Smith, D.L.,
1263 Stanton, R.J., Minczuk, M., Lehner, P.J., et al. (2016). Human Cytomegalovirus Infection
1264 Upregulates the Mitochondrial Transcription and Translation Machineries. mBio *7*,
1265 e00029. https://doi.org/10.1128/mBio.00029-16.

1266 85. Pichlmair, A., Kandasamy, K., Alvisi, G., Mulhern, O., Sacco, R., Habjan, M., Binder, M.,
1267 Stefanovic, A., Eberle, C.-A., Goncalves, A., et al. (2012). Viral immune modulators perturb
1268 the human molecular network by common and unique strategies. Nature *487*, 486–490.
1269 https://doi.org/10.1038/nature11289.

1270 86. Rozenblatt-Rosen, O., Deo, R.C., Padi, M., Adelmant, G., Calderwood, M.A., Rolland, T.,
1271 Grace, M., Dricot, A., Askenazi, M., Tavares, M., et al. (2012). Interpreting cancer genomes
1272 using systematic host network perturbations by tumour virus proteins. Nature *487*, 491–
1273 495. https://doi.org/10.1038/nature11288.

1274 87. Jean Beltran, P.M., Mathias, R.A., and Cristea, I.M. (2016). A Portrait of the Human
1275 Organelle Proteome In Space and Time during Cytomegalovirus Infection. Cell Systems *3*,
1276 361-373.e6. https://doi.org/10.1016/j.cels.2016.08.012.

1277 88. Walter, Z., Li, M., Molho, M., Berish, L., Isopi, A., O'Mara, M., Dittmar, M., Nwaezeapu, C.,
1278 Richards, A., McCullagh, M., et al. (2025). An integrated proteomics approach identifies
1279 phosphorylation sites on viral and host proteins that regulate West Nile virus infection.
1280 Cell Rep *44*, 115728. https://doi.org/10.1016/j.celrep.2025.115728.

1281 89. Rajasekharan, S., Torres, V.A.B., Gomes, Y.C.P., Wilken, L., Overhoff, K., Lin, Y.-C., Patten,
1282 S.A., Watanabe, S., Chatel-Chaix, L., and Scaturro, P. (2025). A genus-wide interaction atlas
1283 across NS4B orthologues identifies a conserved role for UFMylation in orthoflavivirus
1284 replication. Preprint at bioRxiv, https://doi.org/10.1101/2025.05.15.653649
1285 https://doi.org/10.1101/2025.05.15.653649.

1286 90. Perez-Riverol, Y., Bandla, C., Kundu, D.J., Kamatchinathan, S., Bai, J., Hewapathirana, S.,
1287 John, N.S., Prakash, A., Walzer, M., Wang, S., et al. (2025). The PRIDE database at 20 years:
1288 2025 update. Nucleic Acids Res *53*, D543–D553. https://doi.org/10.1093/nar/gkae1011.

1289 91. Schindelin, J., Arganda-Carreras, I., Frise, E., Kaynig, V., Longair, M., Pietzsch, T., Preibisch,
1290 S., Rueden, C., Saalfeld, S., Schmid, B., et al. (2012). Fiji: an open-source platform for
1291 biological-image analysis. Nat Methods *9*, 676–682. https://doi.org/10.1038/nmeth.2019.

1292 92. Verschueren, E., Von Dollen, J., Cimermancic, P., Gulbahce, N., Sali, A., and Krogan, N.
1293 (2015). Scoring Large Scale Affinity Purification Mass Spectrometry Datasets with MIST.
1294 Curr Protoc Bioinformatics *49*, 8.19.1-8.19.16.
1295 https://doi.org/10.1002/0471250953.bi0819s49.

1296 93. Teo, G., Liu, G., Zhang, J., Nesvizhskii, A.I., Gingras, A.-C., and Choi, H. (2014). SAINTexpress:
1297 improvements and additional features in Significance Analysis of Interactome software. J
1298 Proteomics *100*, 37–43. https://doi.org/10.1016/j.jprot.2013.10.023.

1299 94. Gordon, D.E., Jang, G.M., Bouhaddou, M., Xu, J., Obernier, K., White, K.M., O'Meara, M.J.,
1300 Rezelj, V.V., Guo, J.Z., Swaney, D.L., et al. (2020). A SARS-CoV-2 protein interaction map
1301 reveals targets for drug repurposing. Nature *583*, 459–468.
1302 https://doi.org/10.1038/s41586-020-2286-9.

1303 95. Kuznetsov, D., Tegenfeldt, F., Manni, M., Seppey, M., Berkeley, M., Kriventseva, E.V., and
1304 Zdobnov, E.M. (2023). OrthoDB v11: annotation of orthologs in the widest sampling of
1305 organismal diversity. Nucleic Acids Research *51*, D445–D451.
1306 https://doi.org/10.1093/nar/gkac998.

1307 96. Altschul, S.F., Madden, T.L., Schäffer, A.A., Zhang, J., Zhang, Z., Miller, W., and Lipman, D.J.
1308 (1997). Gapped BLAST and PSI-BLAST: a new generation of protein database search
1309 programs. Nucleic Acids Res *25*, 3389–3402. https://doi.org/10.1093/nar/25.17.3389.

1310 97. Ranwez, V., Douzery, E.J.P., Cambon, C., Chantret, N., and Delsuc, F. (2018). MACSE v2:
1311 Toolkit for the Alignment of Coding Sequences Accounting for Frameshifts and Stop
1312 Codons. Mol Biol Evol *35*, 2582–2584. https://doi.org/10.1093/molbev/msy159.

1313 98. Guindon, S., Delsuc, F., Dufayard, J.-F., and Gascuel, O. (2009). Estimating maximum
1314 likelihood phylogenies with PhyML. Methods Mol Biol *537*, 113–137.
1315 https://doi.org/10.1007/978-1-59745-251-9_6.

1316 99. Yang, Z. (2007). PAML 4: phylogenetic analysis by maximum likelihood. Mol Biol Evol *24*,
1317 1586–1591. https://doi.org/10.1093/molbev/msm088.

1318 100. Benjamini, Y., and Hochberg, Y. (1995). Controlling the False Discovery Rate: A Practical
1319 and Powerful Approach to Multiple Testing. Journal of the Royal Statistical Society: Series
1320 B (Methodological) *57*, 289–300. https://doi.org/10.1111/j.2517-6161.1995.tb02031.x.

1321 101. Kosakovsky Pond, S.L., Posada, D., Gravenor, M.B., Woelk, C.H., and Frost, S.D.W. (2006).
1322 GARD: a genetic algorithm for recombination detection. Bioinformatics *22*, 3096–3098.
1323 https://doi.org/10.1093/bioinformatics/btl474.

1324 102. Ebersberger, I., Metzler, D., Schwarz, C., and Pääbo, S. (2002). Genomewide comparison of
1325 DNA sequences between humans and chimpanzees. Am J Hum Genet *70*, 1490–1497.
1326 https://doi.org/10.1086/340787.

1327 103. Shannon, P., Markiel, A., Ozier, O., Baliga, N.S., Wang, J.T., Ramage, D., Amin, N.,
1328 Schwikowski, B., and Ideker, T. (2003). Cytoscape: a software environment for integrated
1329 models of biomolecular interaction networks. Genome Res *13*, 2498–2504.
1330 https://doi.org/10.1101/gr.1239303.

1331 104. Meng, E.C., Goddard, T.D., Pettersen, E.F., Couch, G.S., Pearson, Z.J., Morris, J.H., and
1332 Ferrin, T.E. (2023). UCSF ChimeraX: Tools for structure building and analysis. Protein Sci
1333 *32*, e4792. https://doi.org/10.1002/pro.4792.

1334